applied sciences

MDPI

Review

^{129}Xe: A Wide-Ranging NMR Probe for Multiscale Structures

Matteo Boventi, Michele Mauri and Roberto Simonutti *

Department of Materials Science, Università degli Studi di Milano-Bicocca, Via R. Cozzi 55, 20125 Milano, Italy; m.boventi@campus.unimib.it (M.B.); michele.mauri@unimib.it (M.M.)
* Correspondence: roberto.simonutti@unimib.it

Abstract: Porous materials are ubiquitous systems with a large variety of applications from catalysis to polymer science, from soil to life science, from separation to building materials. Many relevant systems of biological or synthetic origin exhibit a hierarchy, defined as spatial organization over several length scales. Their characterization is often elusive, since many techniques can only be employed to probe a single length scale, like the nanometric or the micrometric levels. Moreover, some multiscale systems lack tridimensional order, further reducing the possibilities of investigation. ^{129}Xe nuclear magnetic resonance (NMR) provides a unique and comprehensive description of multiscale porous materials by exploiting the adsorption and diffusion of xenon atoms. NMR parameters like chemical shift, relaxation times, and diffusion coefficient allow the probing of structures from a few angstroms to microns at the same time. Xenon can evaluate the size and shape of a variety of accessible volumes such as pores, layers, and tunnels, and the chemical nature of their surface. The dynamic nature of the probe provides a simultaneous exploration of different scales, informing on complex features such as the relative accessibility of different populations of pores. In this review, the basic principles of this technique will be presented along with some selected applications, focusing on its ability to characterize multiscale materials.

Keywords: Xe NMR; nanoscale; microscale; porous materials; hierarchical materials; morphology

Citation: Boventi, M.; Mauri, M.; Simonutti, R. ^{129}Xe: A Wide-Ranging NMR Probe for Multiscale Structures. *Appl. Sci.* **2022**, *12*, 3152. https://doi.org/10.3390/app12063152

Academic Editor: Giuseppina Andreotti

Received: 2 March 2022
Accepted: 17 March 2022
Published: 19 March 2022

1. Introduction

The element xenon was first discovered by Ramsay and Travers in 1898 through the study of liquefied air, shortly after the discovery of krypton and neon. Ramsay proposed to call this new element *xenon* after the Greek word ξένον, meaning foreign, strange. Like all the other noble gases, xenon is odorless, colorless, and dense. For a very long time, it was considered completely unable to form chemical compounds, but, in 1962, Bartlett managed to produce the first known xenon compound, xenon hexafluoroplatinate, by mixing Xe with PtF_6, a powerful oxidizing agent. Since then, many other xenon compounds were discovered, such as fluorides, oxides, oxyfluorides, and complexes with carbon, nitrogen, and metal ions, making this element interesting for inorganic chemistry. Nowadays, xenon is obtained commercially in the distillation of liquid air. It is used in specialized light sources, in ion propulsion systems in spacecrafts, and as a general anesthetic.

Natural xenon consists of seven different stable isotopes. Among them, ^{129}Xe is particularly interesting thanks to its relatively high natural abundance (26.4%) and its nuclear spin, I, which is equal to 1/2. In addition to that, with 54 electrons, xenon has a very large electron cloud that makes it a highly polarizable atom, extremely sensitive to the surrounding environment. Thanks to these combined features, this nucleus is very suitable for nuclear magnetic resonance (NMR) spectroscopy: any change in its electron cloud is reflected in its chemical shift value which covers a range of approximately 7500 ppm. Another interesting isotope is ^{131}Xe since it also has a high natural abundance, around 21.2%. However, this nucleus has a nuclear spin of 3/2 and, thus, a nonzero quadrupolar moment which leads to complex spectra even for the simplest materials. Consequently, ^{129}Xe is by far the most used isotope for xenon NMR spectroscopy.

In the 1980s, Ito and Fraissard found that the chemical shift of xenon adsorbed in zeolites was highly influenced both by the size of the cavities and the presence of cations [1,2]. Since these pioneering works, ^{129}Xe NMR spectroscopy has become a very important technique for studying porous species such as zeolites [3–7], mesoporous silica [8,9], organic porous materials [10,11], polymers [12–16], metal organic frameworks [17,18], and, more recently, ionic liquids [19–23]. Several different models for determining the size of the pores via the ^{129}Xe chemical shift have been developed. In addition to that, this technique has proven capable of studying pore connectivity, pore blocking, and hierarchical materials, and to distinguish between different nanosegregated domains and to determine their sizes.

Even though many reviews have been published on this technique [24–29], especially in recent years [30,31], to the best of our knowledge there are no reviews focused on the characterization of materials between the nano and the micro scale. These materials, often constituted by a hierarchical arrangement of nanostructures, have proven to be very interesting both in practical applications and in providing deep insight into transport phenomena. The characterization of these materials is particularly challenging: microscopy needs to be specifically tuned to explore these dimensions and the use of techniques such as conventional NMR and XRD has proven difficult due to the high sensitivity needed to properly characterize the structure and the organization of these materials. In this context, ^{129}Xe NMR spectroscopy, exploiting the high sensitivity of the xenon nucleus to the surrounding environment as well as its inherent mobility, has established itself as a very useful technique, capable of giving detailed information regarding porous structure, morphology, hierarchy, presence and size of different domains, and phase separation.

The first part of this review aims to provide the reader with a general overview of this powerful technique, covering the basic principles, the models proposed to determine the pore sizes of different materials, and some technical details. In the second part, several examples of applications are highlighted, demonstrating how this technique can be used to characterize a wide variety of materials.

2. Basic Principles and Models

2.1. Chemical Shift

In the most established description of the chemical shift of ^{129}Xe adsorbed in a porous material, it is expressed as the sum of different contributions:

$$\delta = \delta_0 + \delta_{\text{Xe-Xe}}\rho_{\text{Xe}} + \delta_{\text{S}} + \delta_{\text{SAS}} + \delta_{\text{E}} + \delta_{\text{M}} \quad (1)$$

δ_0 is the chemical shift of xenon gas at zero pressure, which is conventionally set to 0 ppm and used as reference. This value can be determined by measuring the dependence of the chemical shift of free xenon gas on pressure and extrapolating to zero. The dependence of δ_0 on temperature can be neglected in the standard temperature operating range [32]. The second term corresponds to the chemical shift increase arising from xenon–xenon interactions. This term is directly proportional to xenon density, ρ_{Xe}, and, as such, it can be neglected if the density is sufficiently small. In microporous materials, such as zeolites, this term is particularly significant: by definition, micropores have diameters below 2 nm, and, since the Xe atom has a van der Waals diameter of 0.44 nm, xenon–xenon interactions inside these pores are very relevant. Instead, in mesoporous materials, which have pore diameters between 2 nm and 50 nm, this term can generally be neglected, unless experiments are performed at very high xenon pressures. This second term is generally strongly dependent on temperature [32].

δ_{S} derives from the interaction of xenon atoms with the surface and it is fundamental in studying porous materials and their free volume. The numerous proposed models for determining pore sizes and their distributions via ^{129}Xe chemical shift mainly focus on this term. δ_{S} is temperature dependent as well: the mobility of xenon atoms is increased with increasing temperature and their residence time on the surfaces reduced. Thus, generally speaking, this term decreases with increasing temperature.

δ_{SAS} depends on the interaction of xenon with strong adsorption sites (SAS) such as highly charged or paramagnetic cations. The interaction of xenon with SAS can easily be recognized by analyzing the dependence of the chemical shift on xenon concentration. At very low xenon concentrations, in the presence of strong adsorption sites, the chemical shift increases significantly with decreasing xenon concentration, giving rise to a characteristic hyperbolic dependence [33]. This chemical shift increase is due to the predominance of the δ_{SAS} term: at very low concentrations, most of the xenon atoms interact with this type of site. In the absence of SAS, this term can be neglected, and the chemical shift generally decreases with decreasing xenon concentration, even at low concentration values. δ_E and δ_M are contributions induced by the local electrical fields generated by charged species and by paramagnetic nuclei, respectively. These terms can be omitted in the absence of the corresponding species, greatly simplifying the equation.

Equation (1) gives a quantitative relationship between the various contributions given by the surrounding environment and the xenon chemical shift. However, the xenon atoms can exchange quickly between different adsorption sites and the gas phase in the NMR time scale. The resulting chemical shift is an average of the chemical shifts of xenon atoms in different environments, weighted by the respective molar fractions. Several methods for distinguishing between different sites and obtaining the corresponding chemical shift values have been developed, as will be discussed below. Since every material has its own peculiarities and morphological characteristics, there is no general theory for this approach, and appropriate models have to be determined depending on the material under study. Alternatively, Jokisaari et al. proposed to immerse the porous material under study in a liquid or solid medium [34,35]. This slows down the diffusion of xenon atoms, allowing signals characteristic of a single type of pore to be obtained. This technique has been called "xenon porometry" [36,37].

In most cases, in ^{129}Xe NMR spectra, isotropic signals are observed since the various terms are averaged to their isotropic values. In the case of strongly confined systems or single-file diffusion, anisotropic signals might be observed, and the symmetry of the pores can be derived by analyzing the shape of the signals.

2.2. Proposed Models

2.2.1. Zeolites

As stated previously, zeolites are among the first materials studied employing ^{129}Xe NMR, with the pioneering works about this technique mainly focused on this type of porous structures. In 1987, Demarquay and Fraissard proposed the first model for determining the pore sizes of these materials using the xenon chemical shift. The model was determined by combining experimental and computational approaches on Y, A, L, and Z type zeolites and ferrierite [38]. The relationship between the chemical shift of xenon interacting with the surface, δ_S, and its mean free path, $\bar{l}$, was written as:

$$\delta_S = \delta_a \left(\frac{a}{a + \bar{l}} \right) \quad (2)$$

where δ_a is the chemical shift of the adsorbed xenon and a is a coefficient that depends on the material. It can immediately be seen that $\delta_S = \delta_a$ for $\bar{l} = 0$, and $\delta_S = 0$ for $\bar{l} \rightarrow \infty$, which represents a situation analogous to that of free gas. By fitting the experimental data to this equation, Demarquay and Fraissard determined both δ_a and a:

$$\delta_S = 243 \left(\frac{2.054}{2.054 + \bar{l}} \right) \text{ ppm} \quad (3)$$

where both a and $\bar{l}$ are in Å. Since the studied materials were decationized zeolites or zeolites containing only alkali-metal cations, the terms δ_{SAS}, δ_E and δ_M from Equation (1) can be neglected. Moreover, at sufficiently low xenon pressures, the terms arising from Xe-Xe collisions can also be neglected, making it straightforward to obtain δ_S. Neverthe-

less, by analyzing variable pressure data, it is possible to obtain the pore geometry and, consequently, the pore diameter. In spherical cavities, the distribution of Xe-Xe collisions is isotropic and, thus, the relationship between δ and pressure is linear. On the other hand, in cylindrical pores, the distribution is anisotropic, and δ shows a nonlinear dependence with pressure, with a concavity at high chemical shift values. Knowing the shape of the pores, it is possible to determine their diameter by using the mean free path obtained from Equation (3). For cylindrical pores:

$$D_c = \bar{l} + D_{Xe} \quad (4)$$

while, for spherical pores:

$$D_s = 2\bar{l} + D_{Xe} \quad (5)$$

where D_{Xe} = 4.4 Å.

2.2.2. Mesoporous Silica

In 1993, a model for determining the parameters of the porous structure of mesoporous silica gels was proposed by Mastikhin, Mudrakovski and Terskikh [8]. Their objective was to explain unexpectedly high ^{129}Xe chemical shift values obtained by analyzing various mesoporous silicas (again, in the absence of strong adsorption sites and paramagnetic species). Indeed, from a series of experiments, they obtained values similar to those obtained by Fraissard on zeolites, i.e., around 100 ppm, while working in roughly the same pressure range. Since both nitrogen adsorption and mercury porosimetry did not reveal the presence of micropores, the authors concluded that the model proposed for zeolites was not applicable for this type of material, having average pore sizes in the range 20–400 Å.

They proposed that such scale is wide enough that xenon in the center of the pore behaves as free gas. The actual chemical shift is the result of a dynamic equilibrium between that population and the population adsorbed on the pore surface. Assuming the validity of the ideal gas law inside the pores and assuming that xenon gas is adsorbed according to Henry's law, the xenon chemical shift follows the relationship:

$$\delta = \frac{\delta_S}{1 + \frac{V_g}{KSRT}} \quad (6)$$

where R is the gas constant, T is the temperature, K is Henry's constant and V_g/S is the volume-to-surface ratio of the pores occupied by xenon atoms. This equation shows that the xenon chemical shift depends on the parameters of the porous structure and allows their determination, provided that the Henry's constant is known. Equation (6) can also be expressed in terms of the mean pore size, D, with:

$$D = \frac{\eta V_g}{S} \quad (7)$$

where η is a parameter depending on pore geometry: for cylindrical pores, η = 4, for randomly packed spheres of equal sizes, η = 2.8, and, for slit-like pores, η = 2. These values assume a model with non-intersecting pores, and, formally, lower values must be used in the case of intersecting pores.

By combining Equations (6) and (7), one obtains:

$$\delta = \frac{\delta_S}{1 + \frac{D}{K\eta RT}} \quad (8)$$

It must be remembered that the Henry's constant, K, is in fact temperature dependent. Thus, Equations (6) and (8) are valid only in isothermal conditions. Nonetheless, the

energetic parameters of xenon adsorption can be determined by analyzing the temperature dependence of ^{129}Xe chemical shifts. The Henry's constant can be expressed as:

$$K = \frac{K_0}{\sqrt{T}} e^{\frac{\Delta_{ads}H}{RT}} \quad (9)$$

where K_0 is a temperature-independent pre-exponent and $\Delta_{ads}H$ is the heat of adsorption of the pores under study. Note that, in some papers, the similarity of notation between K and K_0 created a certain confusion. By combining Equations (6) and (9), the following correct relationship is obtained:

$$\delta = \frac{\delta_S}{1 + \frac{V_g}{K_0 SR\sqrt{T}} e^{-\frac{\Delta_{ads}H}{RT}}} \quad (10)$$

This equation can be fit to variable temperature data to obtain the enthalpy of xenon adsorption.

2.2.3. Porous Carbon Materials

Porous carbon materials are generally characterized by disordered structures, heterogeneous surfaces, conductivity, and presence of paramagnetic impurities. These factors strongly influence the interaction of xenon with this type of material and, consequently, its chemical shift.

In 2006, Fraissard and co-workers proposed a model specifically tailored for microporous carbons [39]. By analyzing the chemical shift values of xenon adsorbed into activated carbons with different pore sizes, they found a linear relationship between $\delta_{Xe\text{-}Xe}$ and the mean pore size, D:

$$\delta_{Xe\text{-}Xe} = \eta + \kappa D \quad (11)$$

where $\delta_{Xe\text{-}Xe}$ is expressed in ppm cm^3 mmol^{-1}, η = 5.1 ppm cm^3 mmol^{-1}, and κ = 7 ppm cm^3 mmol $^{-1}$ nm^{-1}. It is important to notice that the authors used $\delta_{Xe\text{-}Xe}$ as the experimental parameter for their model. Indeed, no correlation was found between the chemical shift extrapolated at zero pressure (δ_S) and the mean pore size, contrary to the models described above.

In a later work, a similar approach was followed for mesoporous carbons [40]. Assuming that all the xenon was located on the surface of the materials, it was observed that the chemical shift followed the relationship:

$$\delta(\gamma) = \delta_S + \delta^{Surf.}_{Xe\text{-}Xe}\gamma \quad (12)$$

where γ is the surface density, and the second term describes the binary xenon–xenon collisions on the material surface. $\delta^{Surf.}_{Xe\text{-}Xe}$ was derived by the slope of $\delta(\gamma)$, and the variation of this term with the mean pore size was found to roughly follow the relationship:

$$\delta^{Surf.}_{Xe\text{-}Xe} = \frac{\vartheta}{1 + \xi D} \quad (13)$$

where ϑ = 70 ppm m^2 μmol^{-1} and ξ = 0.5 nm^{-1}.

2.2.4. Xenon Dissolved in Polymers

In 1993, Miller et al. proposed a model for the chemical shift of xenon dissolved in polymers above the glass transition temperature [41]. They assumed that, in these particular materials, xenon experiences a liquid-like environment and, consequently, that its chemical shift can be attributed to solute–solvent interactions. Thus, they described the chemical shift in terms of van der Waals interactions, not considering the bulk susceptibility of the polymers, their magnetic anisotropy, and their permanent electric dipole moment. In their model, xenon is treated as a large diffusant molecule inside a polymer matrix,

which is not only able to occupy the intrinsic free volume of the polymer but also to carve its own pockets thanks to the fluid-like behavior of the rubbery chains. By considering that, in these materials, free volume fluctuates rapidly and, generally, xenon has a high diffusion coefficient, the average free volume environment experienced by xenon atoms in the NMR time scale was modeled, and its van der Waals interaction with the neighboring polymer chains was described using a Lennard-Jones 6–12 potential. Taking into account the diameter of the polymer chains, their equilibrium spacing and the spacing induced by the presence of a diffusant molecule, they were able to calculate the theoretical chemical shifts of xenon in a series of polymers. The applicability of the model was confirmed by experimental data on various samples such as polyethylene (PE), poly(vinyl ethylene) (PVE), polydimethylsiloxane (PDMS), and many other polymers.

The importance of this model lies in the representation of the environment experienced by xenon in the NMR time scale: in polymers, it is extremely different from rigid materials, such as silica and zeolites, widely studied at the time, in which the porosity is static and stable over time. In addition to that, this model shows that each polymer has its own characteristic ^{129}Xe chemical shift, which can be used to characterize polymers and polymer blends as well as to monitor phase separation in these materials, as will be shown in Section 5.2.

3. Hyperpolarization of ^{129}Xe

Thermally polarized ^{129}Xe has been employed as the conventional probe since the first works in the 1980's. Samples with high surface area and/or high xenon adsorption capacities were analyzed with good signal-to-noise ratios without the need of excessively long acquisition times. Variable pressure studies were also conducted to extract the chemical shift of xenon interacting with the surface, δ_S, often reaching low xenon pressures. In these conditions, the ^{129}Xe NMR analysis of materials with low surface area or weak xenon adsorption was strongly limited by the low sensitivity of the technique.

In 1991, Pines et al. reported the successful use of optical pumping of gaseous Rb atoms to strongly enhance the polarization of ^{129}Xe nuclei [42]. This is one of the first and most important examples of hyperpolarized ^{129}Xe NMR. Nowadays, hyperpolarization allows the sensitivity of ^{129}Xe NMR to be enhanced up to 10^4 times compared to the use of thermally polarized xenon. In addition to that, the longitudinal relaxation times can be greatly reduced. These two combined features allow to study a wide variety of materials with low acquisition times and high sensitivity.

Hyperpolarized ^{129}Xe can also transfer its spin polarization to other nuclei, such as ^{1}H and ^{13}C [43,44]. This phenomenon can be exploited to characterize functionalized surfaces and in magnetic resonance imaging (MRI).

There are several methods to obtain hyperpolarized (HP) ^{129}Xe. A brief description of the different possibilities is given below. Further details can be found in the literature [30,31,45].

3.1. Spin Exchange Optical Pumping

The most common method for the creation of HP ^{129}Xe is spin exchange optical pumping (SEOP) [46,47]. In this approach, gaseous Rb, obtained at 100–150 °C in a glass cell, is placed in a magnetic field and irradiated with circularly polarized light at a wavelength of 794.4 nm, corresponding to the D_1 line of Rb. This creates a polarized non-Boltzmann population of Rb atoms. Then, a mixture containing xenon, nitrogen, and helium is brought into contact with the rubidium gas. The electronic polarization of Rb atoms is transferred to the xenon nuclei via the formation of van der Waals Rb-Xe pairs. Nitrogen is added to the gas mixture to quench the fluorescence of the alkaline gas atoms, preventing the loss of polarization. The production of HP ^{129}Xe via SEOP can be carried out both in batch and in continuous modes.

3.2. Dynamic Nuclear Polarization

The hyperpolarization of xenon nuclei can be achieved via dynamic nuclear polarization (DNP), as demonstrated in 2015 by Comment and co-workers [48]. In this technique, at a temperature around 1.2 K, the electron spin polarization of stable organic radicals is transferred to xenon nuclei by irradiating the system with microwaves close to or at the EPR frequency of the free radicals [49]. Xenon is then brought to room temperature and used for the analysis. The enhancement in sensitivity given by this technique is comparable to that of SEOP.

3.3. Brute Force Method

As an alternative to SEOP and DNP, the hyperpolarization of xenon nuclei can also be achieved by the so-called brute force method, using high magnetic fields and temperatures on the order of millikelvins. As a first example, Krujkov et al. reported the production of hyperpolarized xenon at a temperature of 25 mK and in a 14.7 T magnetic field [50]. The main problem of this method is the long T_1 of solid xenon in this temperature range.

4. Experimental Details

Even though ^{129}Xe NMR is a somewhat exotic technique, its implementation is straightforward. The preparation of the samples is quite simple, and spectra can be acquired using conventional NMR instruments. However, as stated previously, this is not the case for HP ^{129}Xe NMR, which requires a complex apparatus (see Section 3 and references therein). This small section provides the reader with some technical details regarding sample preparation and data acquisition.

4.1. Sample Preparation

For conventional ^{129}Xe NMR measurements, samples are in the form of sealed NMR glass tubes (usually 5 mm or 10 mm outer diameter) with gaseous xenon inside. It is important to select tubes with increased wall size, depending on the required final pressure. Prior to the preparation, samples must be degassed under vacuum, at a high temperature if necessary, to remove air and other adsorbed species. This can be done directly inside the NMR tube. Then, xenon gas is inserted inside the tube with a proper apparatus, for example a Schlenk line, and kept inside by freezing with liquid nitrogen. Lastly, the tube containing xenon and the sample is hermetically sealed, either with a flame or with a valve.

In HP ^{129}Xe NMR, instead, the sample is directly placed into the NMR tube and inserted into the instrument. In this case, Magic Angle Spinning (MAS) probes and rotors can also be used, because the hyperpolarized xenon gas is produced and delivered directly into the sample, eliminating the need of using sealed tubes. No further preparation is required.

4.2. Data Acquisition

^{129}Xe NMR data can be acquired with conventional NMR instruments. Both 5 mm and 10 mm broadband probes can be used, provided that they can be tuned on the ^{129}Xe Larmor frequency, which is close to that of ^{13}C. For example, in a 11.7 T magnet, where ^{1}H resonates at 500 MHz, the Larmor frequencies of ^{13}C and ^{129}Xe are 125.8 and 139.1 MHz, respectively. Spectra are normally acquired without spinning, even with solid samples and MAS probes.

Many different NMR techniques can be applied, such as one pulse experiments, measurement of relaxation times, 2D exchange spectroscopy (EXSY) and pulsed field gradient (PFG) NMR. The application of these techniques to ^{129}Xe NMR experiments will be illustrated in the next sections.

5. Applications

As stated previously, materials between the nano and the microscale often show unique properties not directly dictated by their chemical composition but by their structure, which

represents a higher level in the complex organization of these materials. Thus, it is often necessary to create materials with precise shape, orientation, and arrangement, making the desired properties emerge from their structure. Moreover, many materials are constituted by the multiscale arrangement of nanostructures or building blocks, which is an even higher level in the structural hierarchy. This complexity makes it difficult to properly characterize these materials, since the characterization techniques need to be sensitive to different levels of their organization. Among the different possible techniques, ^{129}Xe NMR is especially suitable for this purpose thanks to its high sensitivity to the local environment, which allows probing of the matter on different levels, providing highly detailed information about morphology and dynamics. Below, some selected applications of this technique are presented, starting from the basic information that can be extracted from different kinds of systems and, then, focusing on its ability to give structural information both on the nano and on the microscale.

5.1. Liquids, Mixtures, and Solutions

The highly polarizable electron cloud of xenon is strongly altered when this species is dissolved in liquid phases. Naturally, this is reflected in its NMR signal, which, analogously to solid materials, can be used to obtain in-depth structural and morphological information along with knowledge about phase separation, dynamics, and presence and size of different domains. Owing to these important features, ^{129}Xe NMR has been used to study a variety of pure liquids, mixtures, solutions, and host–guest complexes in the liquid phase [51–57].

Ionic liquids (ILs) can be defined as salts whose melting point is below 100 °C [58]. In the last two decades, they have attracted much attention thanks to their unique physical properties, such as thermal stability [59], outstanding solvent properties [60], and the possibility to tailor their properties by carefully choosing their constituents [61,62]. Even though they are often treated as simple solvents, they are complex structured materials whose properties are frequently associated to their organization on the nano and on the micro scales [63]. A thorough structural and morphological characterization of ionic liquids is mandatory to obtain important structure–property relationships, useful both in understanding the characteristics of these materials and in designing task-specific ionic liquids. The structure of a series of 1-alklyl-3-methylimidazolium-based ionic liquids has been studied in 2013 with ^{129}Xe NMR [19]. Xenon dissolved in ionic liquids gave chemical shifts in the broad range between 150 and 250 ppm (Figure 1), with a very strong dependence on the nature of the anion, a weak temperature dependence in the range 305–340 K, and a negligible xenon pressure dependence. Chemical shift data were correlated to the average size of the cages probed by xenon in the NMR time scale, using the calculated average cage size for xenon in benzene as a reference (5.3 Å, chemical shift δ = 188.1 ppm). The average cage size increased when going from halide anions to bulky, noncoordinating anions, such as $[TfN_2]^-$. Good agreement was also found between these results and the crystal structure data found in literature.

In another recent work, the dynamics of xenon in 1-alkyl-3-methylimidazolium chloride and hexafluorophosphate ionic liquids were studied combining NMR and molecular dynamics [64]. Pulsed gradient spin echo experiments allowed the diffusion coefficients of ^{129}Xe, ^{19}F, and ^{1}H to be measured. The calculated ^{129}Xe diffusion coefficient was about an order of magnitude smaller than that of ^{129}Xe in water (2.2×10^{-9} m^2 s^{-1}) and in alkanes, and it increased with increasing the alkyl chain length, while the diffusion coefficients of ^{19}F and ^{1}H followed an opposite trend. This indicated that the influence of the structural organization of ILs on the dynamics of these species was significantly different. The increase in viscosity with the alkyl chain length caused a decrease in the mobility of the anion–cation components. On the other hand, the extension of the nonpolar components favored xenon diffusion, with a much more significant increase in the Cl^- ILs. These results pointed to the existence of segregated polar and nonpolar domains, the size and interconnectivity of the latter increasing with the alkyl chain length, creating more free volume easily accessible by xenon and, consequently, enhancing its diffusion.

Moreover, it was observed that the nanosegregation was stronger in chloride salts with respect to hexafluorophosphate salts. Interestingly, different results were obtained in a later work where bis(trifluoromethanesulfonyl)imide (TFSI) was chosen as the anion part: xenon diffusion coefficients slightly decreased with increasing the alkyl chain length [65]. In this case, MD studies proved that xenon interacted significantly with the flexible and hydrophobic (due to the large charge delocalization) anion. In addition to that, some anions were observed to diffuse in the alkyl domains, making nanosegregation much less defined than in $[C_nC_1im][Cl]$ ILs. The blurred nanodomain separation and, consequently, the possibility for xenon to explore all the possible environments, made its diffusion dependent on the properties of the overall ionic liquid matrix. Thus, the ^{129}Xe diffusion coefficient decreased with increasing viscosity, following the typical trend of the diffusion of small species in liquids.

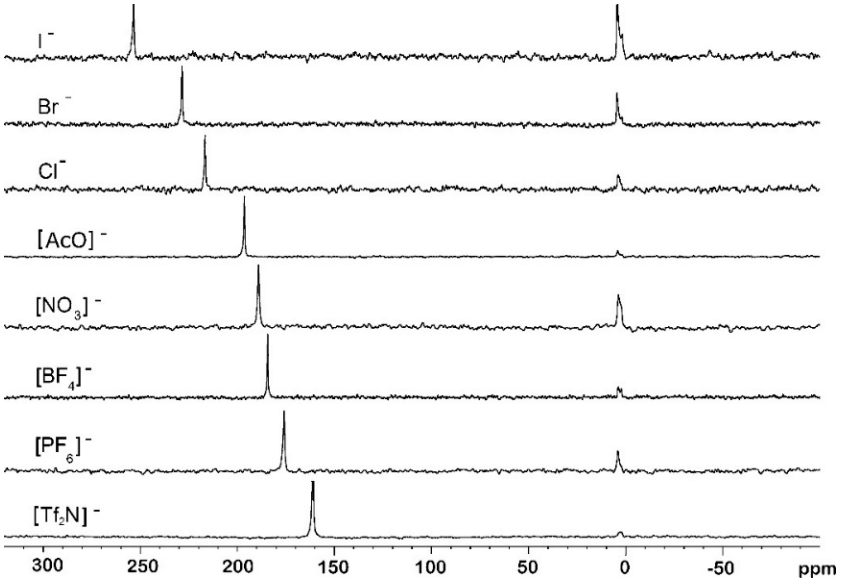

Figure 1. ^{129}Xe nuclear magnetic resonance (NMR) spectra of xenon dissolved in 1-butyl-3-methylimidazolium-based ionic liquids. The anions are indicated on the left. Reprinted with permission from reference [19]. Copyright 2013 American Chemical Society.

The formation of nanosegregated domains has also been recently demonstrated for an hexane/perfluorohexane mixture [66] and for different perfluoroalkylalkanes, which are diblock molecules with the general formula $F(CF_2)_n(CH_2)_mH$ [67]. A theoretical chemical shift of dissolved xenon was calculated assuming a coordination sphere representative of the composition of the bulk, or, in other words, containing a proportion of functional groups interacting with xenon equal to their bulk concentration. Experimental data showed systematic deviations from these values, indicating a shift in the local composition of the mixture compared to the average composition. This, in turn, indicated the nanosegregation between fluorinated and hydrogenated domains, with xenon atoms interacting preferentially with the latter. These results were also confirmed by molecular dynamics simulations.

A thorough study on the liquid organization of a series of hydrocarbons has been performed with ^{129}Xe NMR by Filipe and co-workers [68]. The chemical shift of dissolved xenon in 21 different molecules (among *n*-alkanes, cycloalkanes, and branched alkanes) was obtained in a wide temperature range. The results were interpreted in terms of solvent density and organization of the chemical groups in the vicinity of the xenon atoms, with the aid of molecular dynamics simulations. For *n*-alkanes, the Xe chemical shift depended on the number and proportion of $-CH_3/-CH_2$ groups, with the former showing the greatest influence. For the branched counterparts, δ also depended on the position of these groups. Lastly, for cycloalkanes, it was determined that the various $-CH_2$ groups did not interact

equally with xenon, leading to overall lower chemical shifts compared to the corresponding linear or branched counterparts.

Bartik et al. used xenon NMR to analyze the cavities of α-cyclodextrin [69]. A series of solutions in H_2O/D_2O 80:20 and dimethyl sulfoxide (DMSO) with various α-CD concentrations were analyzed, and the resulting chemical shifts were interpreted with a three-site model comprising a 1:1 complex between Xe and α-CD, Xe in close environment with the host, and bulk xenon. Fitting of the data to this model provided the true chemical shift of xenon in the host–guest complex, as well as the equilibrium constant of its formation. The latter was an order of magnitude smaller in DMSO compared to the H_2O/D_2O mixture, in agreement with the higher solubility of xenon in this solvent with respect to water. Another study on the complexation of xenon was conducted by Berthault and co-workers on different modified cryptophanes, soluble in water at biological pH [70]. The chemical shift of bound xenon decreased with increasing the cavity size. Moreover, binding constants were extracted from both ^{129}Xe and ^{1}H spectra by signal integration and assuming the formation of a 1:1 complex. Their high values coupled with the low T_1 of xenon in these cages pointed toward a possible application of these complexes in biosensing.

In another interesting sensing application, a complex between xenon and a cryptophane functionalized with a nitrilotriacetic acid (NTA) moiety has been proposed as a sensor for Pb^{2+} and Cd^{2+} [71]. It was observed that, upon adding a small amount (48.5 μM concentration) of these ions to a cryptophane solution in D_2O, specific peaks showed up in the ^{129}Xe NMR spectra, corresponding to xenon in the cryptophane cage with the NTA group chelating different metal ions (Figure 2). The sensitivity was improved by applying the HyperCEST (chemical exchange saturation transfer) method, which allowed the detection of up to nanomolar concentrations of Pb^{2+} ions.

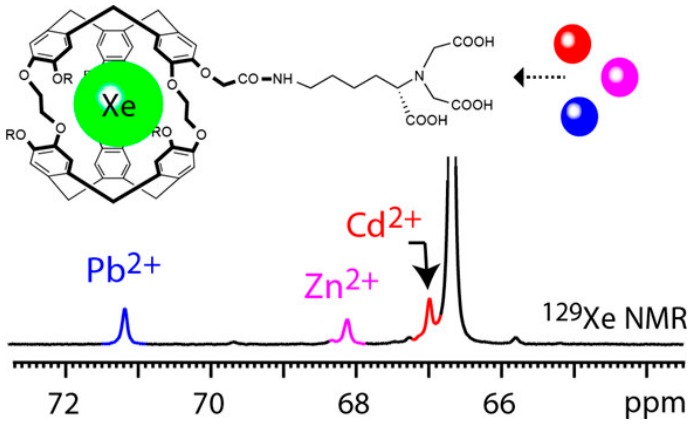

Figure 2. ^{129}Xe NMR spectrum of the cryptophane sensor in the presence of Pb^{2+}, Zn^{2+}, and Cd^{2+} cations, each with a 48.5 μM concentration. Reprinted with permission from reference [71]. Copyright 2014 American Chemical Society.

Complexes of xenon with cryptophanes have also been proposed as pH sensors. In a recent work, two different but similar cryptophanes were used, and the chemical shift difference of the caged xenon atom in the two hosts with respect to the pH was used to construct a calibration curve [72]. Since the curve was constructed from a chemical shift difference and not from a single value, it was shown to be robust against temperature, ionic strength, and solvent effects.

5.2. Polymers

In the late 1980s, researchers began applying ^{129}Xe NMR to polymeric materials by analyzing the spectra of xenon dissolved in the amorphous region of polymers above the glass transition temperature [12]. Since then, this technique has been applied to study several homopolymers [15,41,73], copolymers [13], polymer blends [16,74–77], and crosslinked

polymers [78–80]. Typical diffusion coefficients of Xe dissolved in polymers result in an average displacement of several tens of nm within the NMR experiment timeframe: as a result, Xe is an ideal probe of morphology, dynamics, phase separation, local order, and effects of crosslinking in polymeric materials.

In 2006, continuous flow hyperpolarized xenon NMR was used to study porous PP (polypropylene) and PP/EPR (ethylene propylene rubber) millimeter-sized particles, obtained by polymerization with supported $MgCl_2/TiCl_4$ Ziegler-Natta catalysts [81]. For PP particles, the intensity of the dissolved xenon signal relative to the free gas peak was linearly dependent on temperature, and a temperature of 260 K was extrapolated by this dependence as the temperature at which xenon could not be seen in the polymer structure (Figure 3). This temperature corresponded to the T_g of PP, at which the permeability of xenon in the polymer was too low to detect the signal. Thus, a new way to determine the T_g via continuous flow hyperpolarized ^{129}Xe NMR was proposed. The spectra of PP/EPR particles, instead, showed two distinct peaks corresponding to the two phases, whose dimensions were estimated to be larger than 200 nm on average, considering the difference between the respective xenon chemical shifts and assuming a diffusion coefficient of xenon in the material around 10^{-9} m^2 s^{-1}. Two different glass transition temperatures were obtained by analyzing the relative intensities of the peaks versus the temperature, and their values were very similar to those obtained by differential scanning calorimetry (DSC). 2D EXSY spectra acquired at different mixing times revealed that xenon gas first explored the EPR phase, then the PP phase. From these results, it was concluded that the particles were characterized by a hierarchical structure, with the EPR phase covering the PP phase and preventing direct exchange between the latter and the free gas.

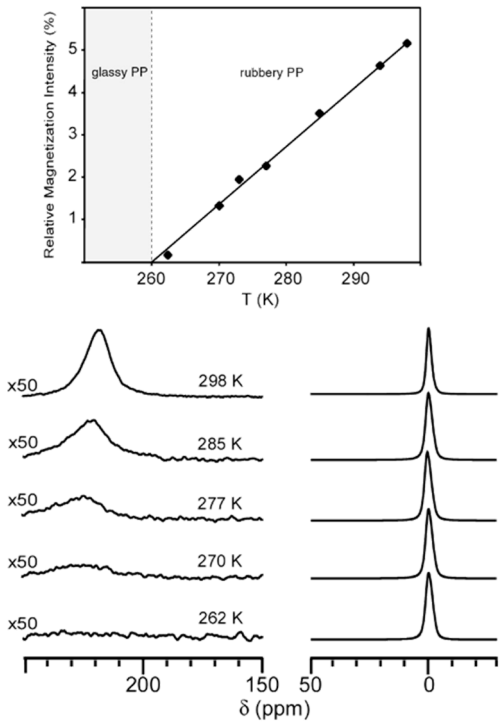

Figure 3. Continuous flow hyperpolarized ^{129}Xe NMR spectra of polypropylene (PP) particles. At the top, the relative intensity of the dissolved xenon signal is reported as a function of temperature. Reprinted with permission from reference [81]. Copyright 2006 American Chemical Society.

An application of xenon NMR has been proposed for the characterization of ultra-high molecular weight polyethylene (UHMWPE) fibers prepared by gel spinning [82]. Equations (3) and (5) were used to estimate the average void size of a series of samples, and this value was found to increase with the tensile modulus of the fibers. Thus, a direct

relationship between the size of the nanovoids in the fibers and their tensile strength was found.

Another interesting application for polymer physics has been illustrated in the study of polyisobutylene (PIB), poly(ethylene-*co*-1-butene) (PEB), and their blends [83]. One-dimensional spectra coupled with pulsed field gradient spin echo experiments allowed the determination of the length scale of mixing in the polymer blends. In 1D spectra, one of the blends, PIB/PEB-66, showed a single peak with a chemical shift in-between those of the corresponding pure components. The PIB/PEB-23 blend instead showed two distinct peaks, indicating that xenon diffused in two different surroundings, characterized by higher length scales of mixing, or domain sizes, compared to the PIB/PEB-66 blend. Xenon diffusion coefficients were used to obtain quantitative data: for the PIB/PEB-66 blend, a length scale of less than 70 nm was calculated, while, for the other blend, it was assumed to be greater than 70 nm (Figure 4).

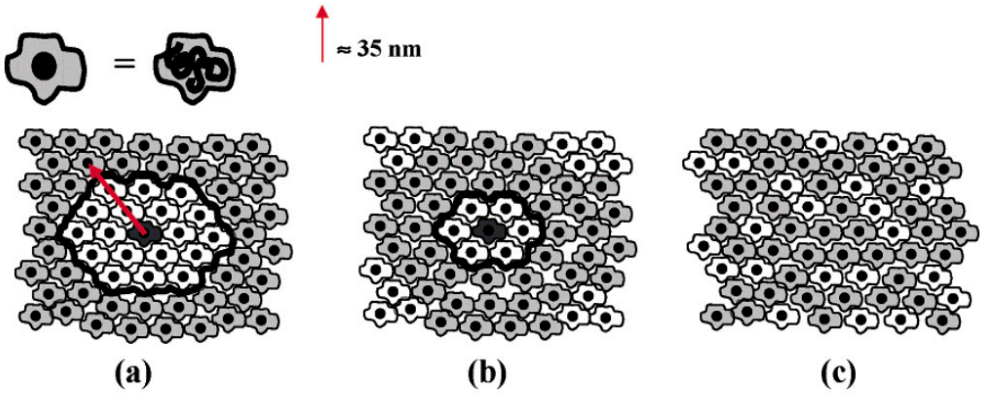

Figure 4. Schematic representation of the mixing length scales of (**a**) the PIB/PEB-23 blend and (**b**) or (**c**) the PIB/PEB-66 blend. For the latter, both representations are possible since the length scale is less than 70 nm in both cases. Reprinted with permission from reference [83]. Copyright 2004 American Chemical Society.

The study of the free volume of polymers can give important information regarding the effects of crosslinking on their morphology, and the high sensitivity of xenon has been exploited for this purpose. For example, in one of the first works on polymers, the presence of four distinct peaks in the range 198.5–201.0 ppm in the spectrum of crude EPDM (ethylene propylene diene monomer) was interpreted as the presence of four physically distinct domains in the amorphous region of the polymer [14]. The chemical shift of these peaks was associated to the relative sizes of these environments: the peak at 198.5 ppm was attributed to the largest free volume, the one at 201.0 ppm indicated the smallest void space, and the intermediate peaks were indicative of phases of in-between sizes. This interpretation was supported by the analysis of the same polymer after sulfur curing: the spectrum was completely different and the peak at 198.5 ppm was no longer observable, consistently with the disappearance of large void spaces due to crosslinking. In another study, a method to determine the crosslink density via xenon NMR data was proposed. A calibration curve of the ^{129}Xe chemical shift versus N_m (average number of monomer units between crosslinks) was constructed for PB (polybutadiene) using swelling data [84]. This curve was then used to determine the degree of crosslinking of the reinforcing PB phase in high-impact polystyrene (HIPS), which was obtained by mixing PB with styrene and starting the polymerization. Indeed, the bonding between polystyrene and the rubbery phase in HIPS made it impossible to determine the crosslink density of PB via direct swelling measurements, while, in ^{129}Xe NMR spectra, signals characteristics of both phases were observed, allowing them to be studied independently.

In a very recent work, the ^{129}Xe NMR analysis of a series of polymeric membranes for CO_2 separation has been reported [85]. Membranes were prepared by photopolymerization

of 2-hydroxyethyl methacrylate, ethylene glycol dimethacrylate, and polymerizable ionic liquids, constituted by a tetraalkylphosphonium cation, containing a vinylbenzene moiety, and variable counter anions. Xenon NMR was performed on the membranes covered in water to keep them wet and to simulate the conditions of typical systems containing CO_2. In the spectra obtained at 30 °C, two downfield signals could be observed for all the samples, as shown in Figure 5 ([P_{nnn}VB] indicates the phosphonium cation containing the vinylbenzene moiety and three linear alkyl chains with n carbon atoms each). The signal at 188 ppm was attributed to xenon in water, while the other one to xenon in the membrane. As can be seen from the (a), (b), and (c) spectra, the chemical shift for poly[P_{nnn}VB][BF4]+acrylates increased when going from ethyl to butyl chains, but then decreased again with further increase of the chain length. This was due to the strong influence of both the relative amount of aliphatic fraction and the terminal -CH_3 groups of the phosphonium cation on the chemical shift. Upon going from ethyl to butyl chains, the increase of the relative aliphatic fraction caused an increase in δ, while, with octyl chains, the strong decrease in the relative amount of terminal -CH_3 groups prevailed, shifting the signal upfield. This interpretation, combined with the even lower chemical shift for the $[Tf_2N]^-$ based membrane, pointed to the existence of different domains whose separation was dependent on the nature of the anion, as demonstrated previously (see Section 5.1). These results were confirmed by ^{13}C SS-NMR, which indicated a much higher mobility for the alkyl chains of the cations compared to the other components.

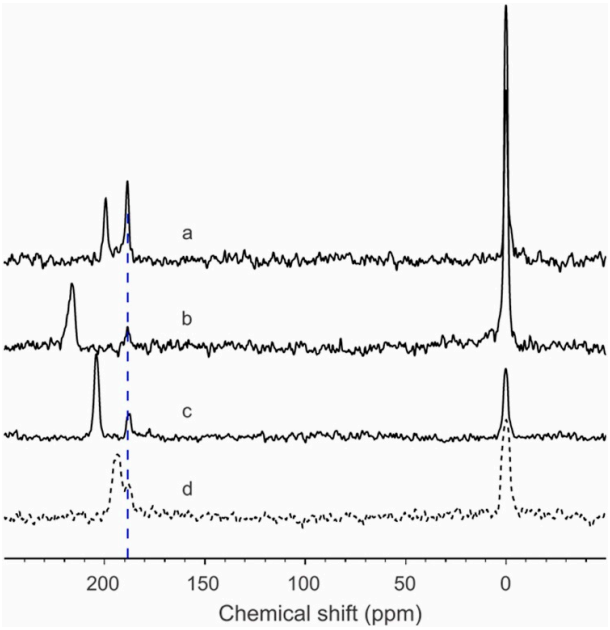

Figure 5. ^{129}Xe NMR spectra obtained at 30 °C of ionic liquid-polyacrylate copolymer membranes: (**a**) poly[P_{222}VB][BF_4]+acrylates, (**b**) poly[P_{444}VB][BF_4]+acrylates, (**c**) poly[P_{888}VB][BF_4]+acrylates, (**d**) poly[P_{888}VB][Tf_2N]+acrylates. The vertical dashed line marks the chemical shift of xenon in water. Reprinted with permission from reference [85]. Copyright 2021 *Journal of Membrane Science*.

Xenon NMR spectroscopy has also been used to characterize polymers below the glass transition temperature. For example, this technique coupled with positron annihilation lifetime spectroscopy (PALS) has been used to study the free volume of a series of glassy perfluorinated polymers [86]. Free volumes were obtained by employing Equations (3)–(5), and the chemical shift values extrapolated at zero xenon pressure. Even though the equations are formally valid only for microporous zeolites, reasonable agreement was found between xenon NMR and PALS data. A comparison between PALS and ^{129}Xe NMR data was also made by Whittaker et al. on poly(2-hydroxyethyl methacrylate) hydrogels [87]. In these samples, the absence of peaks due to xenon in water led to the conclusion that xenon was located in weakly or non-hydrated hydrophobic domains. Moreover, the analysis

of samples prepared with different water contents revealed that the ^{129}Xe chemical shift decreased with increasing water content. This was attributed to an increase in free volume due to the materials progressively passing from a glassy to a rubbery state with increasing water content.

Suzuki et al. studied several other glassy polymeric systems, including poly(2,6-dimethyl-1,4-phenylene oxide) (PPO) [88], PPO/PS blends [89], and tetramethyl bisphenol A polycarbonate (TMPC)/PS blends [90], using ^{129}Xe NMR and Xe sorption measurements. For these studies, the sorption behavior of xenon in glassy polymers was described using a dual-mode adsorption model. The assumption is that xenon dissolves in the polymer matrix via a Henry's mechanism and is adsorbed in the nanovoids via a Langmuir mechanism. This generates two different contributions to the xenon chemical shift: δ_D (dissolved xenon, Henry's mechanism) and δ_H (adsorbed xenon, Langmuir mechanism). The fitting of the xenon adsorption isotherms at various temperatures, along with the analysis of variable temperature and pressure ^{129}Xe NMR spectra, allowed determination of the relative concentrations of xenon atoms in the two different sites, and the corresponding chemical shift values. Lastly, these values were used along with Equation (3) to determine the effective size of the nanovoids.

A widely diffused method for obtaining polymers is emulsion polymerization. This technique allows latexes constituted by homo or copolymer particles to be obtained. The careful selection of the synthetic conditions allows the dimensions and the morphology of the latex particles to be tailored, allowing many different architectures to be obtained [91]. ^{129}Xe NMR has been used as a technique to evaluate the structure and the morphology of various homo- and copolymer particles synthesized by emulsion polymerization [92]. When polymers were analyzed below their glass transition temperature, the slow exchange between xenon inside and outside the particles caused different peaks to appear in the spectra (Figure 6). On the other hand, when temperature was increased above the T_g, as in the case of poly(butyl acrylate-*co*-methyl methacrylate) ($T_g \approx 32$ °C) at 60 °C, a single peak was observed, indicating fast exchange between different environments on the NMR time scale. The analysis of chemical shift and line width data allowed determination of the rate constant of the xenon penetration in the particles, which was observed to be independent on the xenon gas pressure and on the nature of the latex. Thus, it was shown that information regarding the core of the particles and the exchange of xenon between polymer and bulk could be obtained.

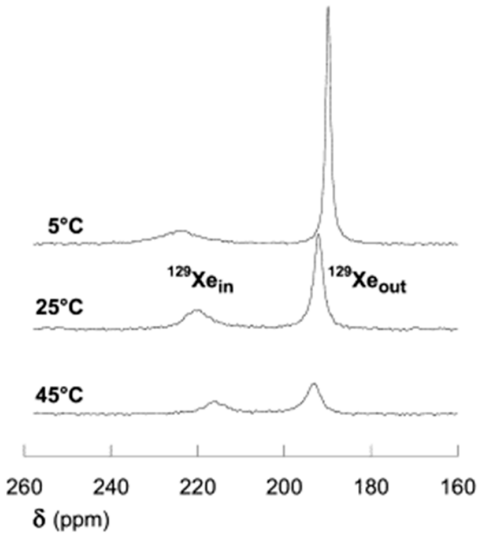

Figure 6. Variable temperature ^{129}Xe NMR spectra of xenon dissolved in a polystyrene colloid below the glass transition temperature (T_g = 107 °C). Reprinted with permission from reference [92]. Copyright 2006 *Journal of Colloid and Interface Science*.

In another work, hyperpolarized ^{129}Xe NMR was used to monitor the mini-emulsion polymerization of styrene [93]. The polymerization was carried out directly in the NMR instrument, and spectra were acquired at different reaction times. By analyzing the dependence of the chemical shift on the time of acquisition, the authors found that this parameter correlated with the monomer/polymer ratio, allowing the direct monitoring of the polymerization. Moreover, this approach allowed the two different kinetic profiles given by two different initiators to be distinguished between. To validate the results, calorimetric data were acquired, and good agreement was observed between these and chemical shift data.

Polymers of intrinsic microporosity (PIMs) are polymers which possess permanent pore sizes below 2 nm due to their rigid and complex structures that do not fill the space efficiently. They can be used for gas storage, gas and liquid separation, preparation of membranes, and sensing [94]. Thorough characterization of their porous structure is crucial in determining their properties and their performances in various applications. In 2010, ^{129}Xe NMR was used to study two spirobifluorene-based PIMs with different linkers [95]. δ_S was extrapolated from variable pressure data and used to determine the average pore diameters, which were <0.8 nm in both cases, showing that the linkers did not have a significant influence on this value. Since the size of the pores created by the structural units of these polymers was predicted to be around 1.2–1.4 nm, the authors concluded that their porous structures were created by interdigitated structural units and deformed pores, possibly generated due to incomplete condensation reactions during the synthesis. Direct comparison between PALS and ^{129}Xe NMR on an ethanoanthracene-based PIM synthesized by Tröger's base formation (PIM-EA-TB) further confirmed the applicability of this technique in the characterization of porosity in this class of materials [96].

5.3. Mesoporous Silica

The extensive study of mesoporous silica by means of ^{129}Xe NMR began in 1993 with the work published by Mastikhin et al., in which Equation (10) was proposed [8]. Afterwards, many other papers on this type of materials were published.

For example, in 2002, a thorough NMR study on ordered mesoporous silica (OMS) materials and their counterparts functionalized with alkyl silanes (referred to as PNNL materials) was conducted by Ripmeester, Exarhos, and co-workers [9]. Nitrogen adsorption measurements and TEM indicated the presence of regular porous channels with different sizes. By performing variable temperature and variable pressure continuous flow hyperpolarized ^{129}Xe NMR, instead, the authors were able to identify the presence of a nonregular and nonuniform porous structure, spacing from micro to mesopores (room temperature spectra are shown in Figure 7). More specifically, xenon was revealed to be in fast exchange between two different nonuniform regions of porosity in the NMR time scale. This provided a much more in-depth level of detail regarding the porous structure of the materials compared to N_2 adsorption and TEM data. Moreover, by analyzing the functionalized materials, they determined that the hydrocarbon chains had two main effects: first, the accessibility of the silica surface was partially blocked; second, xenon dissolved in the hydrocarbon chains, generating broad resonances at around 200 ppm in some spectra. This paper clearly demonstrated the applicability of ^{129}Xe NMR in detecting surface effects and different pore size distributions in silica-based materials. Similar results were obtained in a work on mesoporous silicas functionalized with various ratios of 3-[2-(2-aminoethylamino)ethylamino] propyltrimethoxysilane (AEPTMS) and 3-cyanopropyltriethoxysilane (CPTES) [97]. In addition to distinguishing the effects of functionalization on the mesoporous structure, 2D EXSY spectra of AEPTMS-functionalized silica were analyzed to gain a deeper insight into the interconnectivity of different domains. It was observed that xenon exchanged rapidly between the mesopores and the free gas signal at around 0 ppm, while a longer mixing time was required to observe the exchange between the organic surface phase and the mesopores and between the free gas and the organic phase.

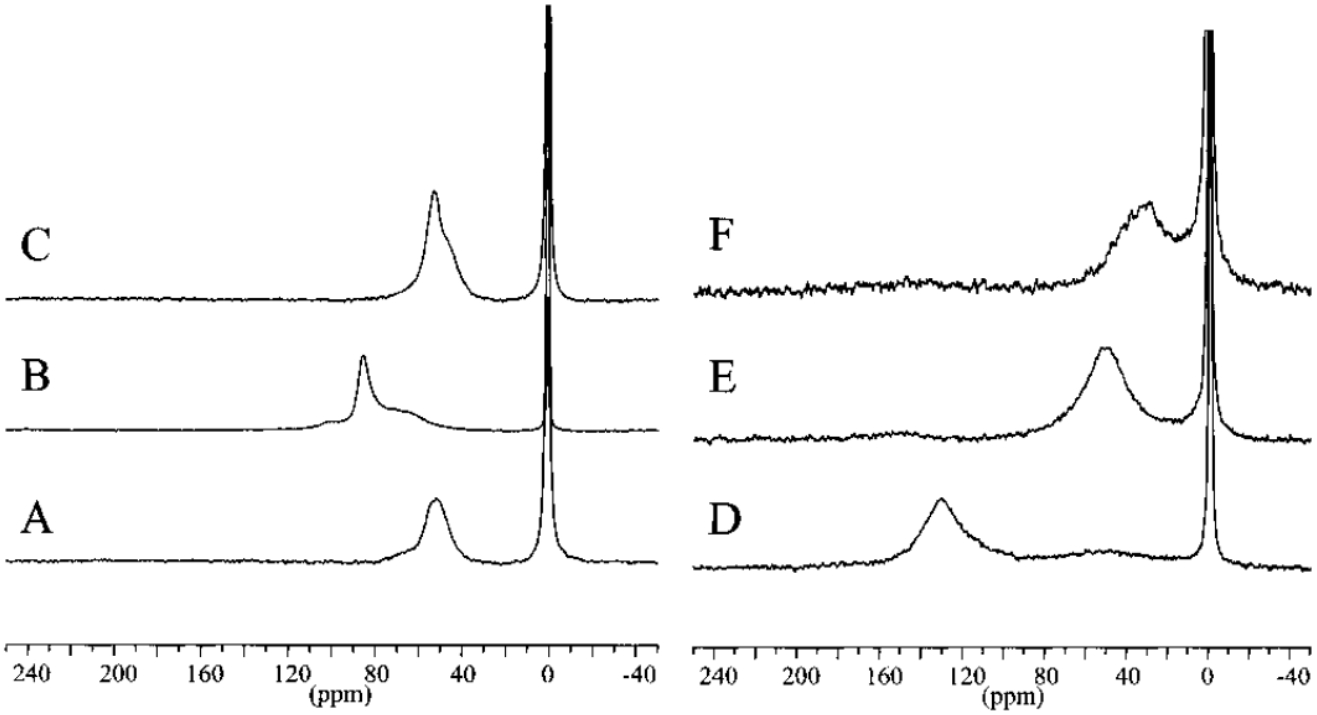

Figure 7. Room temperature continuous flow hyperpolarized ^{129}Xe NMR spectra of ordered mesoporous silica (OMS) materials and their functionalized counterparts (referred to as PNNL) with different pore sizes: 5 nm, 9.3 nm, and 30 nm. (**A**) OMS-5, (**B**) OMS-9.3, (**C**) OMS-30, (**D**) PNNL-5, (**E**) PNNL-9.3, (**F**) PNNL-30. Reprinted with permission from reference [9]. Copyright 2002 American Chemical Society.

HPLC columns are constituted by silica-based materials, often functionalized to enhance their capability to retain apolar compounds, making separation processes more efficient. Some functionalized HPLC materials have been studied employing ^{129}Xe NMR by the group of Ba [98]. In their study, xenon was chosen as a probe molecule representative of a possible mobile phase, and the structure of the stationary phase along with its interaction with xenon was analyzed. By performing a series of variable temperature experiments, the authors were able to distinguish between four different xenon populations: xenon solvated in the stationary phase, xenon in the pores of the silica particles, xenon in the interparticle spaces of the material, and xenon outside the column material. In addition to that, 2D EXSY experiments at low temperatures were performed, directly observing the diffusion of xenon between the interparticle spaces and the pores of the silica particles. In a subsequent work, the authors also applied ^{1}H-^{129}Xe CP NMR experiments to confirm the separation and the distinction between xenon inside the pores and xenon in the interparticle space [99]. Overall, these studies allowed determination of the structure of the column materials, as well as the solvation and the dynamics of xenon atoms, gaining information about the interaction of these materials with apolar species.

Mesostructured silica-based materials containing metallic species can be prepared by synthesizing metal nanoparticles directly inside the mesoporous structure. The resulting metal-containing mesoporous materials can show widely different porous structures, depending not only on the silica-based constituents but also on the shape and size of the metal particles. ^{129}Xe NMR was employed to study Ag-functionalized silica synthesized by templating with octadecyltrimethylammonium bromide (C_{18}TAB) [100]. First, calcined materials not containing silver were analyzed. Contrary to the results obtained by N_2 adsorption, which showed a bimodal distribution of pores, the Xe NMR spectrum showed three distinct resonances at 74, 44 and 10 ppm, along with the typical peak at 0 ppm assigned to free gas. The resonance at 10 ppm was attributed to xenon weakly confined in the

interparticle clusters formed by sintering processes, also observed in TEM images, while the other two peaks indicated other two different pore environments. Thus, this technique revealed fine structural details not detected by conventional adsorption–desorption methods. Ag-functionalized silica again showed three distinct peaks but with two main differences: resonances were shifted downfield at 81, 63 and 22 ppm, respectively, and the signals were much more intense. Since in a previous work it was observed that the interaction of xenon with Ag^+ cations led to strong upfield shifts, sometimes resulting in negative chemical shift values [101], the authors excluded the presence of this species in the synthesized materials. Instead, they attributed the differences to the presence of Ag nanoparticles which reduced the volume of the pores, increasing xenon confinement and, consequently, its chemical shift. An analogous study was conducted in 2016 on rod-shaped silica particles [102]. First, the authors compared the spectra of these materials with spherical silica particles having similar pore sizes, analyzed both before and after compression. The comparison revealed that the single signal observed at 54 ppm for rod-shaped particles, which shifted at 73 ppm upon compressing the material, was indicative of xenon dynamically exchanging between different environments in the NMR time scale, including inter-particle connections and intra-particle mesopores. This fast exchange could only be possible with cylindrical pores open at both ends. Upon compression, the signal shifted to a higher chemical shift value, very similar to that of spherical particles with pores of analogous sizes. This indicated that compressing the sample blocked most of the inter-particle connections, resulting in a signal mostly indicative of xenon inside the porous structure. The analysis of the corresponding Ag-loaded particles revealed that most of the pore structure was occupied by Ag nanoparticles, even though a very small signal could still be observed at 54 ppm, indicating that a small fraction of the pores remained unoccupied (Figure 8).

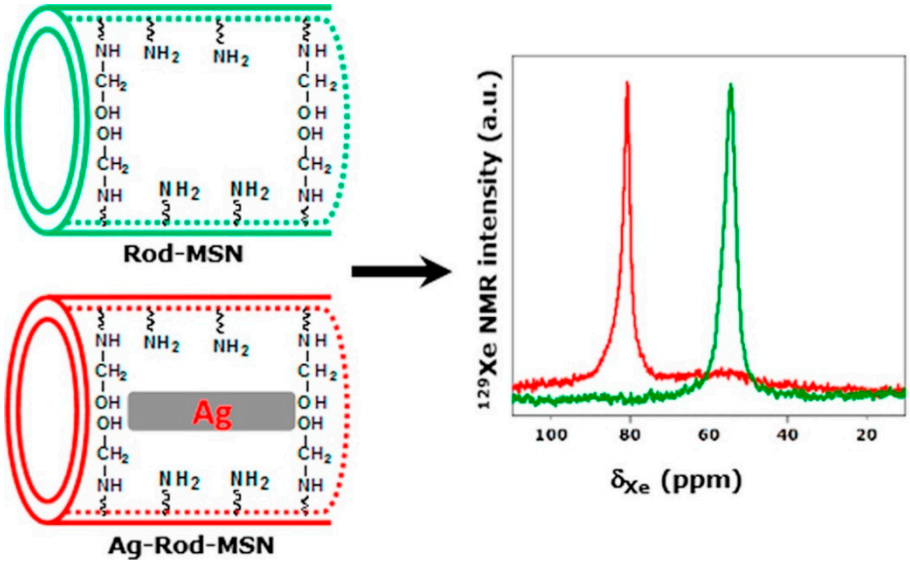

Figure 8. Comparison of the spectra of rod-shaped mesoporous silica particles and their corresponding Ag-loaded counterparts. Reprinted with permission from reference [102]. Copyright 2006 *Journal of Solid State Chemistry*.

Given that ^{129}Xe NMR provides a high level of detail regarding the structure of the analyzed materials, it can also be used to monitor chemically-induced variations in the morphology of the materials and gain insight into the mechanism and the dynamics involved. For example, starting from silica-based materials with a disordered pore structure, it is possible to obtain ordered mesoporous materials such as MCM-41 and MCM-48, with the aid of a surfactant and a structure-directing agent [103]. The degree of transformation can be controlled by the synthetic conditions, allowing the creation of materials with both the original and the newly formed porous structures, and the creation of complex hierarchical

architectures with well-defined morphology. This process, called pseudomorphic synthesis, has been studied with HP ^{129}Xe NMR in the case of the transformation of LiChrospher 60 silica gel and controller pore glasses (CPG) into MCM-41 by analyzing materials with different degrees of transformation [104,105]. The authors were able to distinguish between two different transformation mechanisms for LiChrospher 60 and CPG, respectively. In the former, the signal of the starting pore structure could be detected for up to 50% MCM-41 content, indicating that the original structure was not completely hindered by the presence of MCM-41. Combining these findings with N_2 adsorption data, they determined that, in this case, the transformation proceeded via the formation of distinct MCM-41 domains dispersed over the particles, as illustrated schematically in Figure 9. When CPG was used as the starting material, instead, the signal of the original porosity disappeared even at low conversion values. To better understand this phenomenon, a series of 1D selective EXSY experiments were performed. Even in this case, the signal associated with the starting CPG porosity was not observed, indicating that the MCM-41 component either completely blocked the initial porous structure or significantly slowed down the exchange between the two porous systems. Thus, it was concluded that the transformation preferentially took place in the outer regions of the material, creating a surface layer of MCM-41. The authors attributed the two different mechanisms to the different ability to accommodate the newly formed MCM-41 structure, deriving from the different pore sizes of the starting materials: LiChrospher 60 possesses small mesopores, whereas the studied pore glass had an average pore diameter of 53 nm.

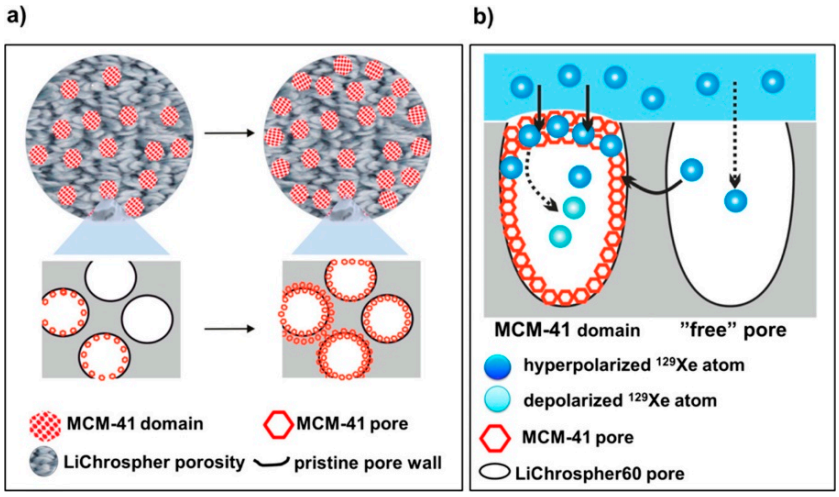

Figure 9. (**a**) Schematic representation of the transformation of LiChrospher 60 into MCM-41. (**b**) Schematic representation of the transport of ^{129}Xe in the partially transformed material. Reprinted with permission from reference [105]. Copyright 2017 American Chemical Society.

Silica aerogels are highly porous and extremely lightweight materials. Their peculiar properties make them suitable for a wide variety of applications, such as thermal and acoustic insulation, energy absorption, catalysis and catalyst support, extraction, fuel storage, and drug delivery [106,107]. These materials are obtained by conventional sol-gel processes followed by aging of the gel and drying. This last step is conducted in particular conditions, such as with supercritical fluids, to preserve the original gel structure to the greatest possible extent. The porous structure of silica aerogels is generally characterized with conventional N_2 adsorption measurements. However, the possibility to alter the porous structure of these materials along with the typical broad pore size distributions represent serious limitations in this type of approach. HP ^{129}Xe NMR can provide in-depth information with minimal or no sample disruption and with high sensitivity. In a very recent work, different hydrophobic silica aerogels were synthesized, and their porous structure was characterized using hyperpolarized xenon NMR [108]. Two series of materials

were prepared with different aging times, employing acid (series A) and basic catalysis (series B), respectively. All the materials showed asymmetric broad peaks in the range 100–150 ppm, indicative of inhomogeneous pore size distributions originated by different pore species (Figure 10). The somewhat high chemical shift values were attributed to the high hydrophobicity of the modified silica gels, which strongly enhances the interaction with xenon, affecting its NMR signal. Consequently, quantitative determination of pore sizes was not conducted. Nonetheless, the spectra clearly showed that the porous structure of the A series was different from that of the B series. This was due to the different reaction mechanisms: acid-catalyzed synthesis created linear chains with overall low degree of crosslinking, whereas basic catalysis increased the degree of crosslinking and created highly branched networks.

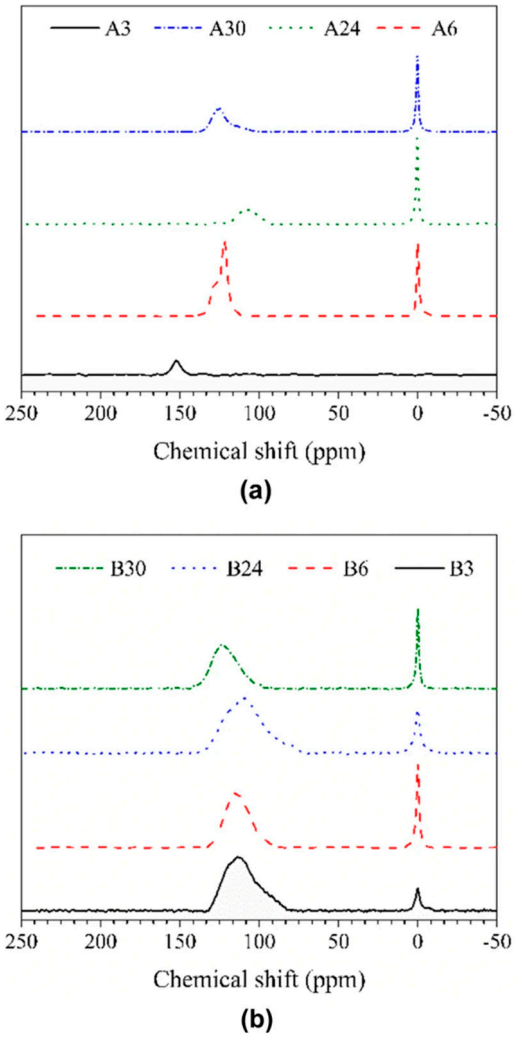

Figure 10. HP ^{129}Xe NMR spectra of hydrophobic silica gels synthesized with (**a**) acid catalysis and (**b**) basic catalysis. The numbers indicate the different aging times. Reprinted with permission from reference [108]. Copyright 2021 *Journal of Sol-Gel Science and Technology*.

^{129}Xe NMR has also been used to characterize the hierarchical structure of dendritic fibrous nanosilica (DFNS) [109], a recently discovered new class of mesoporous silica. A series of variable temperature spectra in the range 173–293 K revealed the existence of two different, non-connected porous structures. Indeed, two separate peaks were observed in the whole temperature range, indicating that no fast exchange between the corresponding xenon populations took place. Combining these data with SAXS, SEM and N_2 adsorption

measurements, the authors concluded that DFNS particles were characterized by a two-level bicontinuous structure.

5.4. Porous Carbon Materials

Compared to zeolites and mesoporous silica, the xenon NMR analysis of porous carbonaceous solids is challenging due to their structural features. Nonetheless, this technique has proven extremely useful even in the characterization of this type of materials. Many different carbonaceous solids have been studied [110–113], and a quantitative model has also been proposed, as outlined before [39,40].

The porous structure of the mesoporous CMK-3 carbon material has been characterized by variable pressure and 2D EXSY hyperpolarized xenon NMR experiments [114]. Excluding the free gas signal, two different peaks were detected in the spectra, and, owing to their chemical shift values and their pressure dependence, they were attributed to two populations of pores of different sizes: micropores and mesopores. The presence of both micropores and mesopores in CMK-3 could be explained by two reasons: (1) presence of two types of carbon particles due to inhomogeneity in the synthetical process, and (2) presence of microporosity in the mesoporous structure or, in other words, presence of a hierarchical structure. 2D EXSY confirmed the second hypothesis: only mesopore-gas and mesopore-micropore cross-peaks were detected at a small mixing time (50 ms), indicating that the gas had to go through the mesoporous structure to reach the smaller micropores (Figure 11). Thus, the presence of a hierarchical structure in CMK-3 was demonstrated for the first time.

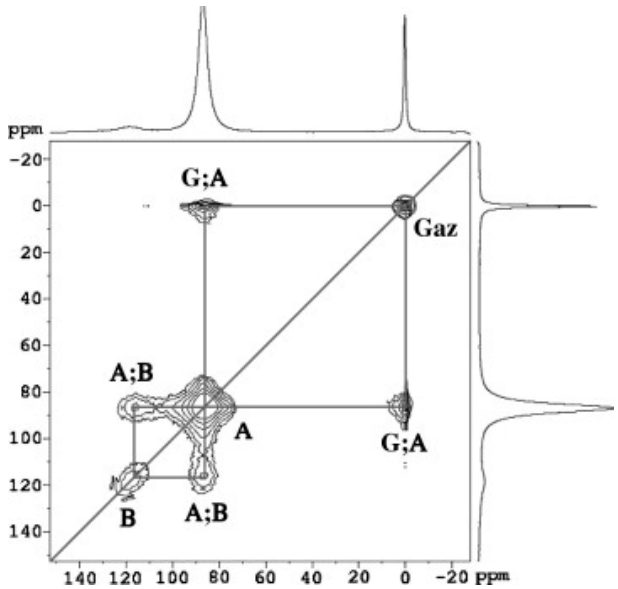

Figure 11. Hyperpolarized ^{129}Xe 2D exchange spectroscopy (EXSY) spectrum of CMK-3 acquired at 293 K and a mixing time of 50 ms. Reprinted with permission from reference [114]. Copyright 2009 Carbon.

Carbon nanotubes (CNT) are among the most attractive carbon-based materials. These materials have shown remarkable performances in terms of electrical conductivity [115], thermal conductivity [116], mechanical strength [117], and gas sensing [118]. CNTs can be divided into two general categories. Single-wall carbon nanotubes (SWCNTs) are single tubes with diameters in the nanometer range, while multi-wall carbon nanotubes (MWCNTs) are constituted by nested single-wall nanotubes held together by weak intermolecular interactions. In 2005, Xe NMR was applied to study the porous structure of single- and multi-wall carbon nanotubes [119]. Even though the adsorption of xenon was weak, the analysis of variable temperature spectra and spin-lattice relaxation times revealed that, in SWCNTs, xenon adsorbed preferentially on the metal impurities, while the slightly stronger

adsorption in MWCNTs was due to the presence of defects, which acted as preferential adsorption sites for xenon. In the same year, xenon adsorption on MWCNTs was also studied by Romanenko et al. [120]. Open and closed nanotubes (as determined by TEM images) were analyzed, and this allowed signals arising from xenon on the outer nanotube surface and xenon located in the interior of the nanotubes to be distinguished between. The weak adsorption of xenon was indicated by a weak pressure dependence of the chemical shift values. Moreover, CNTs were also analyzed after a ball milling process. Both open and closed CNTs displayed a single signal after ball milling, suggesting fast exchange between external and internal xenon atoms, indicating that ball milling opened up the interior volume of the nanotubes. Lastly, variable temperature data were fit to Equation (10) to determine the physical parameters of adsorption.

In 2014, CMK-3 and a series of micro and mesoporous carbide-derived materials were studied with high pressure ^{129}Xe NMR [121]. Using a homemade apparatus, variable pressure spectra were acquired up to 18 bar, and the dependence of the adsorbed xenon chemical shift on the relative pressure was studied. The shape of the resulting curves for different materials resembled adsorption isotherms for micro and mesopores, allowing elucidation of the different porous structures. The chemical shift value extrapolated at a relative pressure of 1 was in good agreement with the pore sizes determined by nitrogen adsorption data. In addition to that, the analysis of the line shapes and linewidths of the materials provided information regarding the width of the pore size distributions and exchange phenomena related to the connectivity between pores. Lastly, spectra were also acquired after the adsorption of *n*-nonane, which was thought to selectively block micropores, leaving mesopores unaltered. Thus, lower chemical shift values for exchange peaks were expected. On the contrary, a slightly higher δ value was observed, as can be seen in Figure 12. This was explained by a reduction in size for the mesopores due to the adsorption of *n*-nonane combined with a stronger xenon–nonane interaction compared to the xenon–wall interaction.

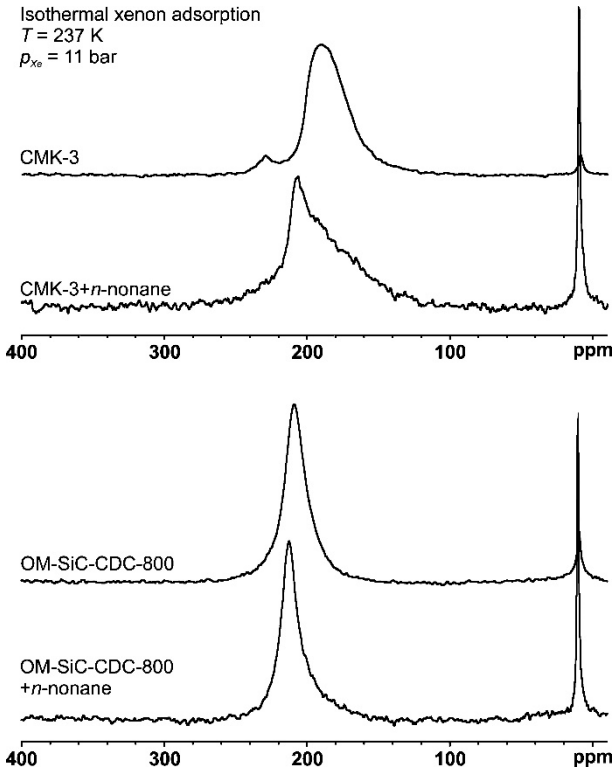

Figure 12. ^{129}Xe NMR spectra of CMK-3 and an ordered mesoporous carbide-based material, taken before and after adsorption of *n*-nonane. Reprinted with permission from reference [121]. Copyright 2014 American Chemical Society.

The conversion of biomasses into activated carbons, called biochar, is a very attractive process which obtains specialty materials with a low environmental impact. These materials have proven useful in wastewater treatment, soil conditioning, catalysis, and as construction materials [122,123]. The activation of biomasses can be achieved via different methods, including pyrolysis and treatment with acids, bases, steam, carbon dioxide, or ionic liquids. These processes deeply change the structure of the starting materials, creating extended porous structures which are responsible for the emerging properties. The porous structures of a series of pecan shell-based biochar were analyzed with ^{129}Xe NMR by Simonutti and co-workers [124]. The spectrum of untreated pecan shells only showed the free gas peak close to 0 ppm, indicating the absence of pores in which confined xenon could be distinguished from the free gas. Biochar prepared with different airflow rates during activation (i.e., different nominal oxygen levels) showed very broad peaks between 100–200 ppm, indicating very broad pore size distributions. A slight upfield shift in the peak apex with increasing airflow rates indicated that higher degrees of oxidation created pores with slightly larger average sizes. 2D EXSY experiments also demonstrated that part of the adsorbed xenon was in exchange with the free gas in a time scale of around 100 ms. More specifically, the detected cross peaks were not centered to the adsorbed xenon peak, but they were shifted toward the rightmost part of the broad signal, indicating that only xenon located in the largest pores was able to exchange with the free gas. In a subsequent work, the same authors studied the porosity of biochar derived from almond shells [125]. Biochar was prepared by treating the almond shells in inert atmosphere at 800 °C and variable times in the range 60–240 min. Some samples were washed with water to remove the ash originated by the thermal treatment. ^{129}Xe NMR spectra revealed that the porosity of the materials increased with increasing treatment duration. Moreover, the spectra of washed materials showed larger and much more intense adsorbed xenon peaks (relative to the free gas peaks) compared to unwashed materials with the same treatment duration. This result revealed that the waste originated from thermal treatments partially obstructed the porous structures of the materials, significantly altering their properties. This was in accordance with BET studies, which showed an increase in surface area both with increasing treatment time and with water washing. In addition to that, 2D EXSY experiments showed that exchange between the free gas and the porous structure occurred only for some of the water washed samples, proving that this process also had a significant impact on pore accessibility.

5.5. Organic Porous Materials

Organic molecules can be used instead of silica to obtain aerogels. For example, it is possible to prepare resorcinol-formaldehyde aerogels via polymerization and consequent drying with supercritical CO_2 [126]. In these materials, the [Resorcinol]/[Catalyst] (R/C) ratio of the starting solution is the main parameter affecting the final gel properties, such as its porous structure. Xenon NMR was used to study aerogels prepared with different (R/C) ratios [10,127]. Room temperature spectra revealed the presence of both mesoporous spaces and a broad distribution of micropores for all R/C ratios. The obstruction of the micropores was also observed by inserting gaseous $CHCl_3$ together with Xe into one of the samples and recording NMR spectra at different times. The spectra immediately after $CHCl_3$ adsorption did not show the signal relative to the micropores. After about 25–30 min following chloroform desorption, the signal reappeared and, after 3 h, the spectra returned to the original state. This confirmed the assignment of the signal to the broad micropore distribution: the small $CHCl_3$ molecules were able to fill the tiny micropores and block xenon atoms. In addition to that, the reappearance of the signal and the return of the spectra to the original state demonstrated that chloroform adsorption did not disrupt the porous structure. Finally, variable temperature data fit to Equation (10) gave the V_g/S ratios for the various materials, which was observed to increase linearly with increasing R/C ratios.

HP ^{129}Xe NMR has also been used to demonstrate single-file diffusion of xenon in organic porous materials, such as tris(*o*-phenylenedioxy)cyclotriphosphazene (TPP) [128].

This study was conducted employing the saturation recovery pulse sequence. Hyperpolarized xenon gas was allowed inside the sample for a sufficient time to completely fill its porous structure. Then, a train of 90° pulses was used to destroy the polarization of the nuclei inside the detection cell. Since the sample was under continuous gas flow, hyperpolarized xenon immediately began refilling the detection cell and diffusing inside the porous structure, replacing saturated xenon. After a buildup time, τ, a final 90° excitation pulse was applied, followed by the actual acquisition, in which only the newly diffused gas was detected. Experiments were performed by varying the buildup time, and the ratio $I_{\text{channel}}(\tau)/I_{\text{gas}}$ was observed to follow the typical trend for single-file diffusion. Moreover, peaks in single pulse spectra showed a positive anisotropy-isotropy-negative anisotropy transition with decreasing temperature and/or increasing xenon concentration (Figure 13). At high temperature/low concentration, xenon mostly interacted with the π electrons of the channel walls, giving rise to a positive and axially symmetric anisotropy with a prevailing $\sigma_{\parallel}$ component. As xenon loading increased or temperature decreased, Xe-Xe van der Waals interactions became progressively more important, transforming the positive anisotropy to a negative anisotropy. Similar results were obtained by Cheng and Bowers on L-alanyl-L-valine nanotubes [129], who were also able to observe xenon atoms entering and exiting these nanotubes via a series of 2D EXSY experiments performed at different exchange times and xenon pressures [130]. Assuming Langmuir adsorption for xenon in nanotubes, the authors fit the dependence of the diagonal and the cross-peaks on the mixing time to appropriate analytical expressions, obtaining the mean desorption rate of xenon from the channels. Even though several approximations were made in the proposed kinetic model, the authors demonstrated that the desorption rate decreased with increasing xenon pressure, in accordance with the decreased mobility of Xe in the channels in a diffusion-limited exchange regime. Single-file diffusion has also been observed in the channels formed by phenylether *bis*-urea macrocycles [131]. In this work, very high chemical shifts, up to 340 ppm, higher than solid xenon (around 300 ppm), were observed due to the very strong distortion experienced by the xenon electron cloud inside the microporous channels. It must be pointed out that single-file diffusion can only be observed in systems with channels long enough, in which xenon resides for the whole duration of the NMR experiment. In this regard, even in these microporous systems, xenon acts as a probe of both the nano-sized diameters of the cavities and the much bigger lengths of the channels.

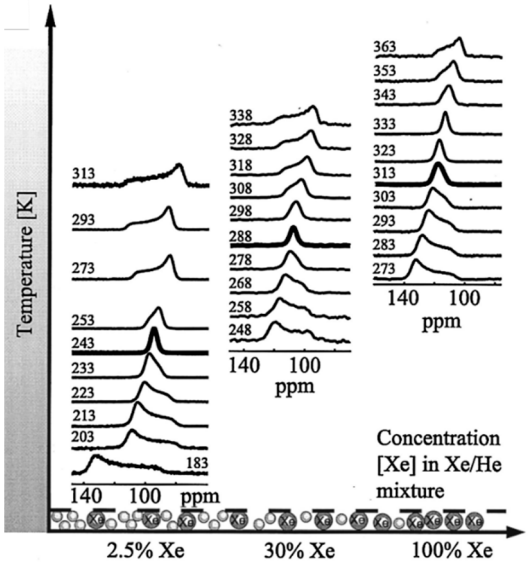

Figure 13. CF HP ^{129}Xe NMR line shapes for Xe inside tris-(*o*-phenylenedioxy)cyclotriphosphazene channels at different temperatures and xenon concentrations. All spectra were acquired at ambient pressure. Adapted with permission from reference [128]. Copyright 2000 American Chemical Society.

In 2017, Telkki et al. studied xenon adsorption and dynamics in the CC3-R molecular cage [132], which showed very good gas separation performances. The CC3-R molecular cage is constituted by four imino-aromatic moieties connected with flexible cyclohexane linkers. Two different sites for xenon adsorption are possible: a cage cavity formed by a single molecule, and a window cavity which is the tunnel between two different, adjacent molecules. Thus, the chemical shift of xenon was assumed to be the result of a weighted average of the shifts relative to these two adsorption sites. A combination of variable pressure (xenon loading) and temperature experiments with computational modeling allowed determination of the δ values for the cage and the window cavities, the relative xenon populations, and the rates of exchange. In addition to that, diffusion coefficients were determined using pulsed gradient stimulated echo (PGSTE) experiments. Two different diffusion components were observed, attributed to inter and intraparticle exchange. The diffusion coefficient relative to intraparticle diffusion decreased rapidly with increasing xenon loading, reflecting the increasing degree of saturation of the porous structure.

Covalent organic frameworks (COFs) have been recently discovered as a new class of crystalline organic materials with a permanent porosity [133]. Like with metal-organic frameworks, it is possible to synthesize stimuli-responsive COFs in which structural changes can be induced by guest molecules, temperature, pressure, or other external factors. Zhang et al. studied the dynamic behavior of a covalent organic framework using variable temperature ^{129}Xe NMR spectroscopy [134]. At high temperatures, only a single broad peak was observed around 220 ppm. A second signal appeared at a higher chemical shift at 248 K, and its relative intensity progressively increased with decreasing temperature. At 193 K, the first signal disappeared and the spectrum showed a single peak around 280 ppm. The same behavior was observed when heating the sample back to 273 K and with increasing xenon pressure. Thus, the two signals were attributed to two different forms of the COF: expanded and contracted. These two forms were also observed with PXRD: spectra demonstrated that solvation with THF induced the transition from the contracted to the expanded form. Unit cell parameters indicated that the latter was able to accommodate more than one xenon atom as opposed to the former. Thus, the signal at high ppm values was attributed to xenon located in the expanded form of the COF, where Xe-Xe interactions were assumed to be significant, while the other signal was assigned to xenon in the contracted form.

In a recent work, hyperpolarized xenon NMR spectroscopy has been used to characterize the morphology of porous starch, a type of synthetically modified starch [135]. Variable temperature and 2D EXSY spectra showed the existence of a mesoporous structure, easily accessible by the free gas, once again giving in-depth information that cannot be obtained via other techniques. In another work, the authors analyzed the adsorption of Pd(II) ions into dithiocarbamate modified mesoporous starch [136]. They were able to determine that these ions preferentially adsorbed into the porous structure of starch and not on its surface.

5.6. Other Materials

Due to the high level of detail provided by xenon NMR spectroscopy, this technique has been used to study the porous structure and connectivity of crystalline mesoporous TiO_2 prepared via a single-step synthesis [137]. Variable temperature hyperpolarized spectra showed two distinct downfield peaks which coalesced at 233 K, indicating the existence of at least two different environments accessible by xenon. With the aid of XRD and TEM, these two environments were determined to be mesopores formed from aggregation of anatase nanoparticles and mesoporous channels constituted by rutile nanorods. Furthermore, their interconnectivity was observed with 2D EXSY experiments acquired at different exchange times.

As an example of the application of ^{129}Xe NMR for the study of naturally occurring porous systems, in 2012, this technique was employed to characterize a series of Italian building stone materials [138]. The porous structures of several different materials were characterized, and the differences were correlated to the mineral composition and to the

microscale characteristics of the samples, as determined by other experimental techniques. Moreover, the spectra of some of the samples showed negative chemical shift signals up to −30 ppm, as can be seen in Figure 14, which were attributed to the presence of transition metal cations, in agreement with the elemental compositions. Lastly, the effects of weathering were studied by freshly cutting one of the samples starting from the bulk material and acquiring spectra at different exposure times to the atmosphere. Significant changes in the porous structure were observed with varying the exposure time, proving that the material adsorbed relevant amounts of atmospheric chemicals, such as water and oxygen.

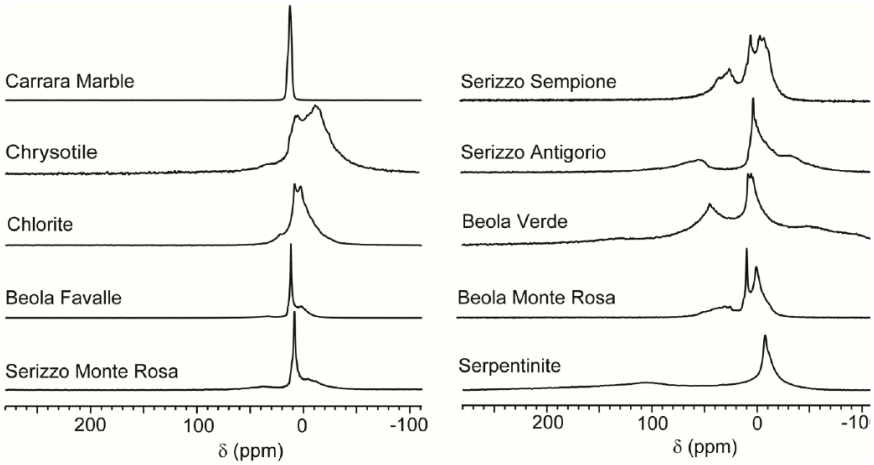

Figure 14. CF HP ^{129}Xe NMR spectra of different building stone materials. Reprinted from reference [138].

In a similar example, Telkki et al. have characterized the porous structures of hydrated cements and Chinese shales [139]. While the cements gave ^{129}Xe signals compatible with the presence of mesopores, the spectra of the shales showed extremely large signals, from about −300 ppm to 300 ppm, with two maxima at −140 ppm and at 50 ppm. This peculiar feature was attributed to the presence of paramagnetic Fe and Mn species. Minerals containing these metals were also detected in the XRD analyses of shale samples. In a subsequent work, shales from USA were analyzed and compared to the Chinese ones [140]. These samples did not show the presence of paramagnetic impurities, contrary to the Chinese shales. Furthermore, from ^{129}Xe NMR spectra, the authors were able to estimate the pore sizes to be between 1 and 10 nm.

Another study on naturally occurring materials was published in 2011 [141]. Porous soil materials and model systems representative of soil components were analyzed using conventional and hyperpolarized ^{129}Xe NMR. These techniques allowed defined and interconnected meso and micropores, structural constrictions (bottle-necks), and multi-domain particle structures to be distinguished.

Mesoporous silicon sponges (MSS) have been recently proposed as anode materials for Li-Ion batteries. Their intrinsic meso/macroporous structure allows to overcome the problem of Si volume expansion during the lithiation process, which leads to the pulverization of silica particles and to a rapid loss of performances of conventional silicon anodes [142]. In 2017, Wang and co-workers employed hyperpolarized ^{129}Xe NMR to characterize a series of MSS with different pore and particle sizes [143]. Spectra acquired at 300 K showed broad peaks for all the materials, indicating the presence of heterogeneous pore size distributions (Figure 15). Moreover, the chemical shift was observed to increase with increasing particle sizes. This result was interpreted in terms of the exchange between the inside and the outside of the particles. Smaller particles displayed a more significant degree of exchange between Xe in the porous structure and the outer surface, reducing the corresponding chemical shift values compared to the larger particles. From a series

of variable temperature experiments and using Equation (10), the authors determined the physical parameters of the adsorption of xenon. The estimated pore sizes, calculated assuming a cylindrical pore model, were much smaller than those derived by SEM, TEM, and nitrogen adsorption. Building on this important information and on the analysis of temperature dependent line shapes and linewidths, it was proposed that the porous structure of the MSS was constituted by mesoporous channels containing small microporous "pockets". The authors performed a similar study on mesoporous silicon sponges grafted with octadecylsilane (H_3Si-C_{18}) in 2018 [144]. It was demonstrated that the grafting process created a thin surface layer (about 2 nm) which covered the micropores embedded in the mesoporous channels, resulting in very different porous structures and interconnectivity compared to those of non-grafted materials.

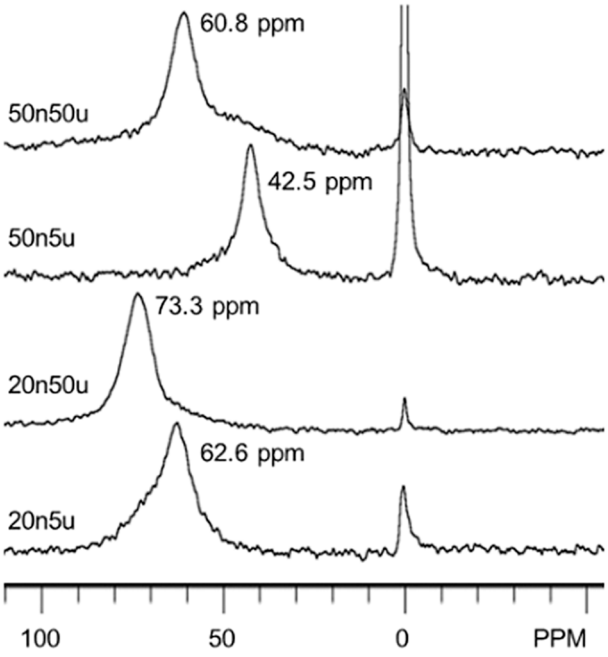

Figure 15. HP ^{129}Xe NMR spectra of various mesoporous silicon sponges acquired at 300 K. The labels indicate pore sizes determined by SEM images (20 nm and 50 nm, respectively) and the particle sizes (5 μm and >50 μm, respectively). Reprinted with permission from reference [143]. Copyright 2017 *Journal of Materials Research*.

Metal chalcogenide aerogels and xerogels can be viewed as assemblies of quantum dots that have both tunable semiconducting properties and intrinsic porosities [145]. Even without varying the chemical composition, the properties of these two types of gel can be drastically different due to the diverse drying processes employed for their preparation, which create completely different structures. The differences in morphology between CdS aerogels and xerogels was explored in 2010 by employing variable temperature hyperpolarized xenon NMR [146]. Aerogels showed peaks attributable to different populations of mesopores, in agreement with nitrogen adsorption data. On the other hand, xerogels could not be analyzed with N_2 adsorption, and only a single resonance at high chemical shift values was observed in a wide range of temperatures, compatible with xenon dissolved in an organic compound. Indeed, thermogravimetric analysis and ^{13}C CP MAS NMR spectra revealed the presence of residual organic compounds from the synthetic process in both gels, with the xerogel containing a much higher amount of them. Thus, the authors concluded that, while the supercritical drying used to obtain the aerogel allowed to maintain a well-defined porous structure, the xerogel collapsed during the drying process. This collapse was only arrested by the organic compounds, which, in turn, occluded the pores of the resulting material.

Multiple-quantum (MQ) NMR has been established as one of the most powerful techniques for the study of materials characterized by anisotropic motions, such as crosslinked polymers and liquid crystals [147]. This technique generally employs complex pulse sequences composed of an excitation block, in which multiple-quantum coherence, dominated by double-quantum (DQ) coherence, is generated, and a reconversion block, with the same pulses but with different phases, that converts multiple-quantum into single-quantum coherences, detectable after a final 90° readout pulse. Ripmeester and co-workers reported the use of a DQ filter in the ^{129}Xe CP MAS NMR analysis of the xenon clathrate of Dianin's compound [148]. This approach allowed the signals of singly and doubly-occupied cavities to be distinguished between, in which ^{129}Xe–^{129}Xe dipolar coupling was measurable since the two nuclei maintained sufficient spatial proximity for the whole duration of the experiment.

Some representative miscellaneous materials recently studied with ^{129}Xe NMR include liquid crystals [149–151], pillared clays [152], and miscellaneous hybrid materials [153–155]. These studies proved how this technique can be successfully employed for the characterization of the most various and most complex materials and systems. In this regard, another representative example is the recent work of Meersmann et al. [156]. Instead of the conventional Xe:He:N_2 mixture for the SEOP production of HP ^{129}Xe, the authors used a Xe:H_2 5:95 mixture. This allowed the use of ^{129}Xe NMR to monitor the temperature changes during the catalytic hydrogenation of propene. More specifically, the authors analyzed the signal of xenon adsorbed in the porous structure of the Pt/Al_2O_3 catalyst as a function of time, under continuous flow of a propene:Xe:H_2 mixture. Time-resolved spectra (Figure 16) showed a rapid decrease of the chemical shift with time in the very first seconds after the start of the reaction, indicating a steep increase in the catalyst temperature in a short amount of time. By comparing the spectral data with a chemical shift-temperature calibration curve constructed previously, the authors concluded that the catalyst reached a temperature of 200 °C in 70 s, contrary to the thermocouple measurement, which indicated that the temperature did not exceed 150 °C. This difference was explained considering that xenon probed the thin outer layer of the alumina pellets, where Pt was located, giving the effective temperature of the reaction locus, contrary to the thermocouple measurement. The steep increase was due to the exothermic nature of the hydrogenation reaction.

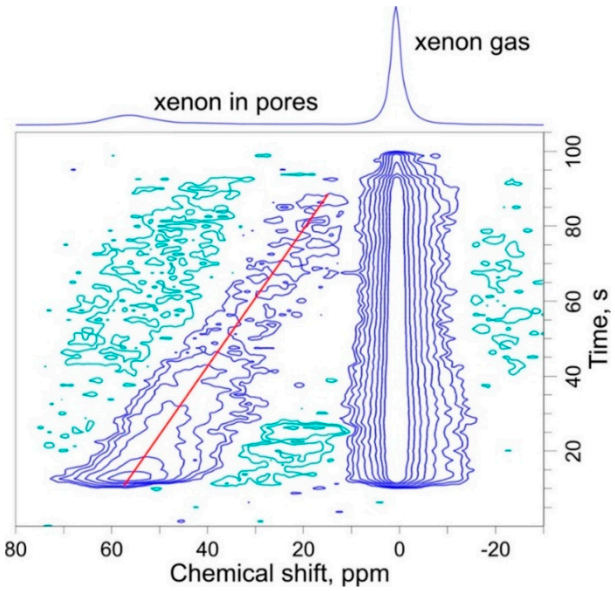

Figure 16. Time-resolved HP ^{129}Xe NMR spectra of Pt/Al_2O_3 pellets under the continuous flow of a propene:Xe:H_2 mixture. Reprinted with permission from reference [156]. Copyright 2020 American Chemical Society.

6. Conclusions

The main goal of this review was to introduce the reader to the innovative applications of ^{129}Xe NMR in the study of complex structures.

The great polarizability of xenon nuclei and its ability to explore different environments can be exploited to obtain in-depth information about morphology, porosity, pore connectivity and blocking, phase separation, and dynamic behavior, for a wide variety of materials. Selected case studies have been illustrated to show how ^{129}Xe NMR can be applied to numerous classes of materials, from pure liquids to structured ionic liquids, from mesoporous silica-based materials to carbonaceous solids, and from polymers to various naturally occurring materials. For other classes of materials, such as zeolites and metal-organic frameworks, the technique is already established and well-reviewed.

Here, instead, special attention has been drawn to its application to a new frontier in complex systems: the study of multiscale and hierarchical structures. Thanks to the high solubility of xenon in apolar environments, coupled with its capability to travel unhindered in a variety of submicrometric volumes, ^{129}Xe NMR is inherently capable to probe a wide range of length scales, from the nanoscale to the higher microscale organization. In this context, typical one-pulse experiments can be combined with more advanced but well-established NMR techniques, like measurement of relaxation times, 2D EXSY or PFG NMR, to simultaneously study different levels in the structural hierarchies and to obtain a detailed picture of the multiscale morphological features of the materials. Moreover, the actual implementation of this technique only requires the preparation of sealed mildly pressurized glass tubes and standard NMR equipment.

With the undergoing development of synthetic multiscale materials, which are still relatively primitive compared to their natural counterparts, there is an increasing need of techniques able to properly characterize their complex structure and support the fast development of synthesis bridging the gap between top-down and bottom-up approaches. In this context, ^{129}Xe NMR, possibly enhanced by hyperpolarization, can emerge among the few innovative techniques standing up to the challenge of multiscale control and optimization.

Author Contributions: Conceptualization, R.S; methodology, M.M.; original draft, M.B.; writing—review and editing, M.B., M.M. and R.S. All authors have read and agreed to the published version of the manuscript.

Funding: M.M. thanks the support from the Italian Ministry of University and Research (MIUR) through the Dipartimenti di Eccellenza—2019 grant.

Institutional Review Board Statement: Not applicable.

Informed Consent Statement: Not applicable.

Conflicts of Interest: The authors declare no conflict of interest.

References

1. Ito, T.; Fraissard, J. *Proceedings of the Fifth International Conference on Zeolites, Naples, Italy, 2–6 June 1980*; Rees, L.V.C., Ed.; John Wiley & Sons: London, UK, 1980; pp. 510–515.
2. Ito, T.; Fraissard, J. ^{129}Xe NMR Study of Xenon Adsorbed on Y Zeolites. *J. Chem. Phys.* **1982**, *76*, 5225–5229. [CrossRef]
3. Fraissard, J.; Ito, T. ^{129}Xe n.m.r. Study of Adsorbed Xenon: A New Method for Studying Zeolites and Metal-Zeolites. *Zeolites* **1988**, *8*, 350–361. [CrossRef]
4. Conner, W.C.; Weist, E.L.; Ito, T.; Fraissard, J. Characterization of the Porous Structure of Agglomerated Microspheres by ^{129}Xe NMR Spectroscopy. *J. Phys. Chem.* **1989**, *93*, 4138–4142. [CrossRef]
5. Ryoo, R.; Pak, C.; Chmelka, B.F. Macroscopic or Microscopic Information of Y Zeolite from ^{129}Xe n.m.r. Line Splitting. *Zeolites* **1990**, *10*, 790–793. [CrossRef]
6. Hartmann, M.; Boddenberg, B. Characterization of CuY Zeolites after Dehydration, and Reduction with Carbon Monoxide Oxidation. *Adsorpt. J. Int. Adsorpt. Soc.* **1994**, *2*, 127–136.
7. Moudrakovski, I.L.; Ratcliffe, C.I.; Ripmeester, J.A. ^{129}Xe NMR Study of Adsorption and Dynamics of Xenon in AgA Zeolite. *J. Am. Chem. Soc.* **1998**, *120*, 3123–3132. [CrossRef]
8. Terskikh, V.V.; Mudrakovskii, I.L.; Mastikhin, V.M. ^{129}Xe Nuclear Magnetic Resonance Studies of the Porous Structure of Silica Gels. *J. Chem. Soc. Faraday Trans.* **1993**, *89*, 4239–4243. [CrossRef]

9. Moudrakovski, I.L.; Terskikh, V.V.; Ratcliffe, C.I.; Ripmeester, J.A.; Wang, L.Q.; Shin, Y.; Exarhos, G.J. A ^{129}Xe NMR Study of Functionalized Ordered Mesoporous Silica. *J. Phys. Chem. B* **2002**, *106*, 5938–5946. [CrossRef]
10. Moudrakovski, I.L.; Ratcliffe, C.I.; Ripmeester, J.A.; Wang, L.Q.; Exarhos, G.J.; Baumann, T.F.; Satcher, J.H. Nuclear Magnetic Resonance Studies of Resorcinol-Formaldehyde Aerogels. *J. Phys. Chem. B* **2005**, *109*, 11215–11222. [CrossRef]
11. Anedda, R.; Soldatov, D.V.; Moudrakovski, I.L.; Casu, M.; Ripmeester, J.A. A New Approach to Characterizing Sorption in Materials with Flexible Micropores. *Chem. Mater.* **2008**, *20*, 2908–2920. [CrossRef]
12. Stengle, T.R.; Williamson, K.L. Nuclear Magnetic Resonance of Xenon Absorbed in Solid Polymers: A Probe of the Amorphous State. *Macromolecules* **1987**, *20*, 1428–1430. [CrossRef]
13. Brownstein, S.K.; Roovers, J.E.L.; Worsfold, D.J. ^{129}Xe Line Widths in Block Copolymers. *Magn. Reson. Chem.* **1988**, *26*, 392–393. [CrossRef]
14. Kennedy, G.J. ^{129}Xe NMR as a Probe of the Effect of Crosslinking on the Amorphous Phase Structure of Solid Polymers. *Polym. Bull.* **1990**, *23*, 605–608. [CrossRef]
15. Kentgens, A.P.M.; van Boxtel, H.A.; Verweel, R.J.; Veeman, V.S. Line-Broadening Effects for ^{129}Xe Absorbed in the Amorphous State of Solid Polymers. *Macromolecules* **1991**, *24*, 3712–3714. [CrossRef]
16. Mansfeld, M.; Flohr, A.; Veeman, W.S. Application of ^{129}Xe NMR to Polymer Blends. *Appl. Magn. Reson.* **1995**, *8*, 573–586. [CrossRef]
17. Hoffmann, H.C.; Assfour, B.; Epperlein, F.; Klein, N.; Paasch, S.; Senkovska, I.; Kaskel, S.; Seifert, G.; Brunner, E. High-Pressure in Situ ^{129}Xe NMR Spectroscopy and Computer Simulations of Breathing Transitions in the Metal-Organic Framework Ni 2(2,6-Ndc)2(Dabco) (DUT-8(Ni)). *J. Am. Chem. Soc.* **2011**, *133*, 8681–8690. [CrossRef]
18. Giovine, R.; Volkringer, C.; Springuel-Huet, M.A.; Nossov, A.; Blanc, F.; Trébosc, J.; Loiseau, T.; Amoureux, J.P.; Lafon, O.; Pourpoint, F. Study of Xenon Mobility in the Two Forms of MIL-53(Al) Using Solid-State NMR Spectroscopy. *J. Phys. Chem. C* **2017**, *121*, 19262–19268. [CrossRef]
19. Castiglione, F.; Simonutti, R.; Mauri, M.; Mele, A. Cage-like Local Structure of Ionic Liquids Revealed by a ^{129}Xe Chemical Shift. *J. Phys. Chem. Lett.* **2013**, *4*, 1608–1612. [CrossRef]
20. Morgado, P.; Shimizu, K.; Esperanc, J.M.S.S.; Reis, M.; Rebelo, P.N.; Lopes, J.N.C.; Filipe, E.J.M. Using ^{129}Xe NMR to Probe the Structure of Ionic Liquids. *J. Phys. Chem. Lett.* **2013**, *4*, 2758–2762. [CrossRef]
21. Saielli, G.; Bagno, A.; Castiglione, F.; Simonutti, R.; Mauri, M.; Mele, A. Understanding Cage Effects in Imidazolium Ionic Liquids by ^{129}XE NMR: MD Simulations and Relativistic DFT Calculations. *J. Phys. Chem. B* **2014**, *118*, 13963–13968. [CrossRef]
22. Brooks, N.J.; Castiglione, F.; Doherty, C.M.; Dolan, A.; Hill, A.J.; Hunt, P.A.; Matthews, R.P.; Mauri, M.; Mele, A.; Simonutti, R.; et al. Linking the Structures, Free Volumes, and Properties of Ionic Liquid Mixtures. *Chem. Sci.* **2017**, *8*, 6359–6374. [CrossRef]
23. Weber, C.C.; Brooks, N.J.; Castiglione, F.; Mauri, M.; Simonutti, R.; Mele, A.; Welton, T. On the Structural Origin of Free Volume in 1-Alkyl-3-Methylimidazolium Ionic Liquid Mixtures: A SAXS and ^{129}Xe NMR Study. *Phys. Chem. Chem. Phys.* **2019**, *21*, 5999–6010. [CrossRef] [PubMed]
24. Dybowski, C.; Bansal, N.; Duncan, T.M. NMR Spectroscopy of Xenon in Confined Spaces: Clathrates, Intercalates, and Zeolites. *Annu. Rev. Phys. Chem.* **1991**, *42*, 433–464. [CrossRef]
25. Barrie, P.J.; Klinowski, J. ^{129}Xe NMR As a Probe for the Study of Microporous Solids: A Critical Review. *Prog. Nucl. Magn. Reson. Spectrosc.* **1992**, *24*, 91–108. [CrossRef]
26. Springuel-Huet, M.A.; Bonardet, J.L.; Gédéon, A.; Fraissard, J. ^{129}Xe NMR for Studying Surface Heterogeneity: Well-Known Facts and New Findings. *Langmuir* **1997**, *13*, 1229–1236. [CrossRef]
27. Ratcliffe, C.I. Xenon Nmr. In *Annual Reports on NMR Spectroscopy*; Academic Press: Cambridge, MA, USA, 1998; Volume 36, pp. 123–221; ISBN 0125053363.
28. Springuel-Huet, M.A.; Bonardet, J.L.; Gédéon, A.; Fraissard, J. ^{129}Xe NMR Overview of Xenon Physisorbed in Porous Solids. *Magn. Reson. Chem.* **1999**, *37*, 1–13. [CrossRef]
29. Raftery, D. Xenon NMR Spectroscopy. In *Annual Reports on NMR Spectroscopy*; Academic Press: Cambridge, MA, USA, 2006; Volume 57, pp. 205–270; ISBN 0125054572.
30. Weiland, E.; Springuel-Huet, M.A.; Nossov, A.; Gédéon, A. ^{129}Xenon NMR: Review of Recent Insights into Porous Materials. *Microporous Mesoporous Mater.* **2016**, *225*, 41–65. [CrossRef]
31. Wisser, D.; Hartmann, M. ^{129}Xe NMR on Porous Materials: Basic Principles and Recent Applications. *Adv. Mater. Interfaces* **2020**, *8*, 1–19. [CrossRef]
32. Jameson, C.J.; Jameson, A.K.; Cohen, S.M. Temperature and Density Dependence of ^{129}Xe Chemical Shift in Xenon Gas. *J. Chem. Phys.* **1973**, *59*, 4540–4546. [CrossRef]
33. Ito, T.; Fraissard, J. ^{129}Xe Nuclear Magnetic Resonance Study of Xenon Adsorbed on Zeolite NaY Exchanged with Alkali-Metal and Alkaline-Earth Cations. *J. Chem. Soc. Faraday Trans. 1 Phys. Chem. Condens. Phases* **1987**, *83*, 451–462. [CrossRef]
34. Telkki, V.V.; Lounila, J.; Jokisaari, J. Determination of Pore Sizes and Volumes of Porous Materials by ^{129}Xe NMR of Xenon Gas Dissolved in a Medium. *J. Phys. Chem. B* **2005**, *109*, 24343–24351. [CrossRef] [PubMed]
35. Telkki, V.V.; Lounila, J.; Jokisaari, J. Behavior of Acetonitrile Confined to Mesoporous Silica Gels as Studied by ^{129}Xe NMR: A Novel Method for Determining the Pore Sizes. *J. Phys. Chem. B* **2005**, *109*, 757–763. [CrossRef] [PubMed]

36. Telkki, V.V.; Lounila, J.; Jokisaari, J. Xenon Porometry at Room Temperature. *J. Chem. Phys.* **2006**, *124*, 034711. [CrossRef] [PubMed]
37. Telkki, V.V.; Lounila, J.; Jokisaari, J. Xenon Porometry: A Novel Method for the Derivation of Pore Size Distributions. *Magn. Reson. Imaging* **2007**, *25*, 457–460. [CrossRef]
38. Demarquay, J.; Fraissard, J. ^{129}Xe NMR of Xenon Adsorbed on Zeolites. Relationship between the Chemical Shift and the Void Space. *Chem. Phys. Lett.* **1987**, *136*, 314–318. [CrossRef]
39. Romanenko, K.V.; Py, X.; De Lacaillerie, J.B.D.E.; Lapina, O.B.; Fraissard, J. ^{129}Xe Nuclear Magnetic Resonance Study of Pitch-Based Activated Carbon Modified by Air Oxidation/Pyrolysis Cycles: A New Approach to Probe the Micropore Size. *J. Phys. Chem. B* **2006**, *110*, 3055–3060. [CrossRef]
40. Romanenko, K.V.; de Lacaillerie, J.-B.D.E.; Lapina, O.; Fraissard, J. Is ^{129}Xe NMR a Useful Technique for Probing the Pore Structure and Surface Properties of Carbonaceous Solids? *Microporous Mesoporous Mater.* **2007**, *105*, 118–123. [CrossRef]
41. Miller, J.B.; Walton, J.H.; Roland, C.M. The NMR Chemical Shift of Xenon-129 Dissolved in Polymers. *Macromolecules* **1993**, *26*, 5602–5610. [CrossRef]
42. Raftery, D.; Long, H.; Meersmann, T.; Grandinetti, P.J.; Reven, L.; Pines, A. High-Field NMR of Adsorbed Xenon Polarized by Laser Pumping. *Phys. Rev. Lett.* **1991**, *66*, 584–587. [CrossRef]
43. Navon, G.; Song, Y.Q.; Rõõm, T.; Appelt, S.; Taylor, R.E.; Pines, A. Enhancement of Solution NMR and MRI with Laser-Polarized Xenon. *Science* **1996**, *271*, 1848–1851. [CrossRef]
44. Rõõm, T.; Appelt, S.; Seydoux, R.; Hahn, E.; Pines, A.; Hahn, E. Enhancement of Surface NMR by Laser-Polarized Noble Gases. *Phys. Rev. B* **1997**, *55*, 11604–11610. [CrossRef]
45. Fan, B.; Xu, S.; Wei, Y.; Liu, Z. Progresses of Hyperpolarized ^{129}Xe NMR Application in Porous Materials and Catalysis. *Magn. Reson. Lett.* **2021**, *1*, 11–27. [CrossRef]
46. Driehuys, B.; Cates, G.D.; Miron, E.; Sauer, K.; Walter, D.K.; Happer, W. High-Volume Production of Laser-Polarized ^{129}Xe. *Appl. Phys. Lett.* **1996**, *69*, 1668–1670. [CrossRef]
47. Walker, T.G.; Happer, W. Spin-Exchange Optical Pumping of Noble-Gas Nuclei. *Rev. Mod. Phys.* **1997**, *69*, 629–642. [CrossRef]
48. Capozzi, A.; Roussel, C.; Comment, A.; Hyacinthe, J.N. Optimal Glass-Forming Solvent Brings Sublimation Dynamic Nuclear Polarization to ^{129}Xe Hyperpolarization Biomedical Imaging Standards. *J. Phys. Chem. C* **2015**, *119*, 5020–5025. [CrossRef]
49. Hyacinthe, J.N.; Capozzi, A.; Comment, A. Chapter 24: Beyond Spin Exchange Optical Pumping: Hyperpolarization of ^{129}Xe via Sublimation Dynamic Nuclear Polarization. In *Hyperpolarized Xenon-129 Magnetic Resonance: Concepts, Production, Techniques and Applications*; Meersmann, T., Brunner, E., Eds.; The Royal Society of Chemistry: Cambridge, UK, 2015; pp. 442–452.
50. Krjukov, E.V.; O'Neill, J.D.; Owers-Bradley, J.R. Brute Force Polarization of ^{129}Xe. *J. Low Temp. Phys.* **2005**, *140*, 397–408. [CrossRef]
51. Miller, K.W.; Reo, N.V.; Schoot Uiterkamp, A.J.M.; Stengle, D.P.; Stengle, T.R.; Williamson, K.L. Xenon NMR: Chemical Shifts of a General Anesthetic in Common Solvents, Proteins, and Membranes. *Proc. Natl. Acad. Sci. USA* **1981**, *78*, 4946–4949. [CrossRef]
52. Diehl, P.; Jokisaari, J. Nuclear Magnetic Relaxation of the ^{129}Xe and 131Xe Isotopes of Xenon Gas Dissolved in Isotropic and Anisotropic Liquids. *J. Magn. Reson.* **1990**, *88*, 660–665. [CrossRef]
53. Moschos, A.; Reisse, J. Nuclear Magnetic Relaxation of Xenon-129 Dissolved in Organic Solvents. *J. Magn. Reson.* **1991**, *95*, 603–606. [CrossRef]
54. Lim, Y.H.; King, A.D. NMR Chemical Shifts of ^{129}Xe Dissolved in Liquid N-Alkanes and Their Mixtures. *J. Phys. Chem.* **1993**, *97*, 555–574. [CrossRef]
55. Luhmer, M.; Moschos, A.; Reisse, J. Intemolecular Dipole-Dipole Spin Relaxation of Xenon-129 Dissolved in Benzene. A Molecular Dynamics Simulation Study. *J. Magn. Reson. Ser. A* **1995**, *113*, 164–168. [CrossRef]
56. Lim, Y.H.; Calhoun, A.R.; King, A.D. NMR Chemical Shifts of ^{129}Xe Dissolved in Liquid Haloalkanes and Their Mixtures. *Appl. Magn. Reson.* **1997**, *12*, 555–574. [CrossRef]
57. Jayapaul, J.; Schröder, L. Probing Reversible Guest Binding with Hyperpolarized ^{129}Xe-NMR: Characteristics and Applications for Cucurbit[n]Urils. *Molecules* **2020**, *25*, 957. [CrossRef] [PubMed]
58. Ghandi, K. A Review of Ionic Liquids, Their Limits and Applications. *Green Sustain. Chem.* **2014**, *04*, 44–53. [CrossRef]
59. Cao, Y.; Mu, T. Comprehensive Investigation on the Thermal Stability of 66 Ionic Liquids by Thermogravimetric Analysis. *Ind. Eng. Chem. Res.* **2014**, *53*, 8651–8664. [CrossRef]
60. Hallett, J.P.; Welton, T. Room-Temperature Ionic Liquids: Solvents for Synthesis and Catalysis. 2. *Chem. Rev.* **2011**, *111*, 3508–3576. [CrossRef]
61. Ahrens, S.; Peritz, A.; Strassner, T. Tunable Aryl Alkyl Ionic Liquids (TAAILs): The next Generation of Ionic Liquids. *Angew. Chem.-Int. Ed.* **2009**, *48*, 7908–7910. [CrossRef]
62. Giernoth, R. Task-Specific Ionic Liquids. *Angew. Chem.-Int. Ed.* **2010**, *49*, 2834–2839. [CrossRef]
63. Canongia Lopes, J.N.A.; Pádua, A.A.H. Nanostructural Organization in Ionic Liquids. *J. Phys. Chem. B* **2006**, *110*, 3330–3335. [CrossRef]
64. Castiglione, F.; Saielli, G.; Mauri, M.; Simonutti, R.; Mele, A. Xenon Dynamics in Ionic Liquids: A Combined NMR and MD Simulation Study. *J. Phys. Chem. B* **2020**, *124*, 6617–6627. [CrossRef]
65. Saielli, G.; Castiglione, F.; Mauri, M.; Simonutti, R.; Mele, A. Xenon Diffusion in Ionic Liquids with Blurred Nanodomain Separation. *ChemPhysChem* **2021**, *22*, 1880–1890. [CrossRef] [PubMed]

66. Morgado, P.; Martins, L.F.G.; Filipe, E.J.M. From Nano-Emulsions to Phase Separation: Evidence of Nano-Segregation in (Alkane + Perfluoroalkane) Mixtures Using ^{129}Xe NMR Spectroscopy. *Phys. Chem. Chem. Phys.* **2019**, *21*, 3742–3751. [CrossRef] [PubMed]
67. Morgado, P.; Barras, J.; Filipe, E.J.M. From Nano-Seggregation to Mesophases: Probing the Liquid Structure of Perfluoroalkylalkanes with ^{129}Xe NMR Spectroscopy. *Phys. Chem. Chem. Phys.* **2020**, *22*, 14736–14747. [CrossRef] [PubMed]
68. Morgado, P.; Bonifacio, R.; Martins, F.G.; Filipe, E.J.M. Probing the Structure of Liquids with ^{129}Xe NMR Spectroscopy: N-Alkanes, Cycloalkanes, and Branched Alkanes. *J. Phys. Chem. B* **2013**, *117*, 9014–9024. [CrossRef] [PubMed]
69. Bartik, K.; Luhmer, M.; Heyes, S.J.; Ottinger, R.; Reisse, J. Probing Molecular Cavities in α-Cyclodextrin Solutions by Xenon NMR. *J. Magn. Reson. Ser. B* **1995**, *109*, 164–168. [CrossRef]
70. Huber, G.; Brotin, T.; Dubois, L.; Desvaux, H.; Dutasta, J.P.; Berthault, P. Water Soluble Cryptophanes Showing Unprecedented Affinity for Xenon: Candidates as NMR-Based Biosensors. *J. Am. Chem. Soc.* **2006**, *128*, 6239–6246. [CrossRef] [PubMed]
71. Tassali, N.; Kotera, N.; Boutin, C.; Léonce, E.; Boulard, Y.; Rousseau, B.; Dubost, E.; Taran, F.; Brotin, T.; Dutasta, J.P.; et al. Smart Detection of Toxic Metal Ions, Pb2+ and Cd2+, Using a ^{129}Xe NMR-Based Sensor. *Anal. Chem.* **2014**, *86*, 1783–1788. [CrossRef]
72. Léonce, E.; Dognon, J.P.; Pitrat, D.; Mulatier, J.C.; Brotin, T.; Berthault, P. Accurate PH Sensing Using Hyperpolarized ^{129}Xe NMR Spectroscopy. *Chem.-A Eur. J.* **2018**, *24*, 6534–6537. [CrossRef]
73. Cheung, T.T.P.; Chu, P.J. Temperature Dependence of ^{129}Xe NMR of Xenon in Polymers. *J. Phys. Chem.* **1992**, *96*, 9551–9554. [CrossRef]
74. Walton, J.H.; Miller, J.B.; Roland, C.M. ^{129}Xe NMR as a Probe of Polymer Blends. *J. Polym. Sci. Part B Polym. Phys.* **1992**, *30*, 527–532. [CrossRef]
75. McGrath, K.J.; Roland, C.M. NMR Study of Miscibility in Polyepichlorohydrin/Poly(Vinylmethylether) Blends. *Rubber Chem. Technol.* **1994**, *67*, 629–635. [CrossRef]
76. Schantz, S.; Veeman, W.S. Nanoheterogeneity in PEO/PMMA Blends Probed by ^{129}Xe-NMR. *J. Polym. Sci. Part B Polym. Phys.* **1997**, *35*, 2681–2688. [CrossRef]
77. Miyoshi, T.; Takegoshi, K.; Terao, T. ^{129}Xe n.m.r. Study of Free Volume and Phase Separation of the Polystyrene/Poly(Vinyl Methyl Ether) Blend. *Polymer* **1997**, *38*, 5475–5480. [CrossRef]
78. Urban, C.; McCord, E.F.; Webster, O.W.; Abrams, L.; Long, H.W.; Gaede, H.; Tang, P.; Pines, A. ^{129}Xe NMR Studies of Hyper-Cross-Linked Polyarylcarbinols: Rigid Versus Flexible Structures. *Chem. Mater.* **1995**, *7*, 1325–1332. [CrossRef]
79. Morgan, D.R.; Stejskal, E.O.; Andrady, A.L. ^{129}Xe NMR Investigation of the Free Volume in Dendritic and Cross-Linked Polymers. *Macromolecules* **1999**, *32*, 1897–1903. [CrossRef]
80. Monguzzi, A.; Mauri, M.; Frigoli, M.; Pedrini, J.; Simonutti, R.; Larpent, C.; Vaccaro, G.; Sassi, M.; Meinardi, F. Unraveling Triplet Excitons Photophysics in Hyper-Cross-Linked Polymeric Nanoparticles: Toward the Next Generation of Solid-State Upconverting Materials. *J. Phys. Chem. Lett.* **2016**, *7*, 2779–2785. [CrossRef]
81. Simonutti, R.; Bracco, S.; Comotti, A.; Mauri, M.; Sozzani, P. Continuous Flow Hyperpolarized ^{129}Xe NMR for Studying Porous Polymers and Blends. *Chem. Mater.* **2006**, *18*, 4651–4657. [CrossRef]
82. Demco, D.E.; Melian, C.; Simmelink, J.; Litvinov, V.M.; Möller, M. Structure and Dynamics of Drawn Gel-Spun Ultrahigh-Molecular-Weight Polyethylene Fibers by 1H, 13C and ^{129}Xe NMR. *Macromol. Chem. Phys.* **2010**, *211*, 2611–2623. [CrossRef]
83. Wachowicz, M.; Wolak, J.; Gracz, H.; Stejskal, E.O.; Jurga, S.; McCord, E.F.; White, J.L. Length Scales Which Perturb Chain Packing in Amorphous Polymers. *Macromolecules* **2004**, *37*, 4573–4579. [CrossRef]
84. Parker, W.O.; Ferrando, A.; Ferri, D.; Canepari, V. Cross-Link Density of a Dispersed Rubber Measured by ^{129}Xe Chemical Shift. *Macromolecules* **2007**, *40*, 5787–5790. [CrossRef]
85. Galiano, F.; Mancuso, R.; Guazzelli, L.; Mauri, M.; Chiappe, C.; Simonutti, R.; Brunetti, A.; Pomelli, C.S.; Barbieri, G.; Gabriele, B.; et al. Phosphonium Ionic Liquid-Polyacrylate Copolymer Membranes for Improved CO_2 Separations. *J. Memb. Sci.* **2021**, *635*, 119479. [CrossRef]
86. Golemme, G.; Nagy, J.B.; Fonseca, A.; Algieri, C.; Yampolskii, Y. ^{129}Xe-NMR Study of Free Volume in Amorphous Perfluorinated Polymers: Comparsion with Other Methods. *Polymer* **2003**, *44*, 5039–5045. [CrossRef]
87. Varcoe, K.M.; Blakey, I.; Chirila, T.V.; Hill, A.J.; Whittaker, A.K. The Effect of Synthetic Conditions on the Free Volume of Poly(2-Hydroxyethyl Methacrylate) as Studied By1H NMR, ^{129}Xe NMR, and Position Annihilation Spectroscopy. *ACS Symp. Ser.* **2007**, *963*, 391–409. [CrossRef]
88. Yoshimizu, H.; Ohta, S.; Asano, T.; Suzuki, T.; Tsujita, Y. Temperature Dependence of the Mean Size of Polyphenyleneoxide Microvoids, as Studied by Xe Sorption and ^{129}Xe NMR Chemical Shift Analyses. *Polym. J.* **2012**, *44*, 821–826. [CrossRef]
89. Suzuki, T.; Yoshimizu, H.; Tsujita, Y. Analysis of Gas Transport Properties of PPO/PS Blends by ^{129}Xe NMR Spectroscopy. *Polymer* **2003**, *44*, 2975–2982. [CrossRef]
90. Yoshimizu, H.; Murakami, T.; Suzuki, T.; Tsujita, Y. Characterization of the Microvoids of a Tetramethyl Polycarbonate/Polystyrene Blend System Using Xe Sorption Measurements and ^{129}Xe NMR Spectroscopy. *Polym. J.* **2012**, *44*, 827–831. [CrossRef]
91. Lovell, P.A.; Schork, F.J. Fundamentals of Emulsion Polymerization. *Biomacromolecules* **2020**, *21*, 4396–4441. [CrossRef]
92. Locci, E.; Roose, P.; Bartik, K.; Luhmer, M. Probing Polymer Colloids by ^{129}Xe NMR. *J. Colloid Interface Sci.* **2009**, *330*, 344–351. [CrossRef]
93. Duewel, M.; Vogel, N.; Weiss, C.K.; Landfester, K.; Spiess, H.W.; Münnemann, K. Online Monitoring of Styrene Polymerization in Miniemulsion by Hyperpolarized ^{129}Xenon NMR Spectroscopy. *Macromolecules* **2012**, *45*, 1839–1846. [CrossRef]

94. Budd, P.M.; Ghanem, B.S.; Makhseed, S.; McKeown, N.B.; Msayib, K.J.; Tattershall, C.E. Polymers of Intrinsic Microporosity (PIMs): Robust, Solution-Processable, Organic Nanoporous Materials. *Chem. Commun.* **2004**, *4*, 230–231. [CrossRef]
95. Weber, J.; Schmidt, J.; Thomas, A.; Böhlmann, W. Micropore Analysis of Polymer Networks by Gas Sorption and ^{129}Xe NMR Spectroscopy: Toward a Better Understanding of Intrinsic Microporosity. *Langmuir* **2010**, *26*, 15650–15656. [CrossRef] [PubMed]
96. Tocci, E.; De Lorenzo, L.; Bernardo, P.; Clarizia, G.; Bazzarelli, F.; McKeown, N.B.; Carta, M.; Malpass-Evans, R.; Friess, K.; Pilnáček, K.; et al. Molecular Modeling and Gas Permeation Properties of a Polymer of Intrinsic Microporosity Composed of Ethanoanthracene and Tröger's Base Units. *Macromolecules* **2014**, *47*, 7900–7916. [CrossRef]
97. Huang, S.J.; Huh, S.; Lo, P.S.; Liu, S.H.; Lin, V.S.Y.; Liu, S. Bin Hyperpolarized ^{129}Xe NMR Investigation of Multifunctional Organic/Inorganic Hybrid Mesoporous Silica Materials. *Phys. Chem. Chem. Phys.* **2005**, *7*, 3080–3087. [CrossRef] [PubMed]
98. Ba, Y.; Chagolla, D. Structure, Dynamics, and Interaction of the Stationary Phase and Xenon Atoms in the Zorbax SB-C18 HPLC Column Material Studied by Solid State NMR and ^{129}Xe NMR. *J. Phys. Chem. B* **2002**, *106*, 5250–5257. [CrossRef]
99. Chagolla, D.; Ezedine, G.; Ba, Y. Solvation, Interaction and Dynamics of Xenon Atoms in HPLC Column Materials Studied by Variable-Temperature Dependent ^{129}Xe, ^{1}H-^{129}Xe Cross-Polarization, and Two-Dimensional Exchange NMR Experiments. *Microporous Mesoporous Mater.* **2003**, *64*, 155–163. [CrossRef]
100. Mnasri, N.; Charnay, C.; De Ménorval, L.C.; Moussaoui, Y.; Elaloui, E.; Zajac, J. Silver Nanoparticle-Containing Submicron-in-Size Mesoporous Silica-Based Systems for Iodine Entrapment and Immobilization from Gas Phase. *Microporous Mesoporous Mater.* **2014**, *196*, 305–313. [CrossRef]
101. Gedeon, A.; Burmeister, R.; Grosse, R.; Boddenberg, B.; Fraissard, J. ^{129}Xe NMR for the Study of Oxidized and Reduced AgX Zeolites. *Chem. Phys. Lett.* **1991**, *179*, 191–194. [CrossRef]
102. Mnasri, N.; Charnay, C.; de Ménorval, L.C.; Elaloui, E.; Zajac, J. Rod-Shaped Silica Particles Derivatized with Elongated Silver Nanoparticles Immobilized within Mesopores. *J. Solid State Chem.* **2016**, *243*, 207–214. [CrossRef]
103. Martin, T.; Galarneau, A.; Di Renzo, F.; Fajula, F.; Plee, D. Morphological Control of MCM-41 by Pseudomorphic Synthesis. *Angew. Chem.-Int. Ed.* **2002**, *41*, 2590–2592. [CrossRef]
104. Uhlig, H.; Hollenbach, J.; Rogaczewski, M.; Matysik, J.; Brieler, F.J.; Fröba, M.; Enke, D. Pseudomorphic Transformation of Porous Glasses into Micelle-Templated Silica. *Chem. Ing. Tech. 2017 89*, 863–875. [CrossRef]
105. Hollenbach, J.; Küster, C.; Uhlig, H.; Wagner, M.; Abel, B.; Gläser, R.; Einicke, W.D.; Enke, D.; Matysik, J. Hyperpolarized ^{129}Xe NMR as an Alternative Approach for Investigating Structure and Transport in Ordered Mesoporous Materials Prepared via Pseudomorphic Transformation. *J. Phys. Chem. C* **2017**, *121*, 15804–15814. [CrossRef]
106. Schmidt, M.; Schwertfeger, F. Applications for Silica Aerogel Products. *J. Non-Cryst. Solids* **1998**, *225*, 364–368. [CrossRef]
107. Gurav, J.L.; Jung, I.K.; Park, H.H.; Kang, E.S.; Nadargi, D.Y. Silica Aerogel: Synthesis and Applications. *J. Nanomater.* **2010**, *2010*, 1–11. [CrossRef]
108. Barboza-Carmona, J.D.; Wenzel, M.; Eckert, L.; Enke, D.; Matysik, J.; Céspedes-Camacho, I.F. A Spectroscopic Insight of the Porous Structure of Hydrophobic Silica Aerogels by Hyperpolarized ^{129}Xe NMR. *J. Sol-Gel Sci. Technol.* **2022**, *101*, 176–184. [CrossRef]
109. Bahadur, J.; Maity, A.; Sen, D.; Das, A.; Polshettiwar, V. Origin of the Hierarchical Structure of Dendritic Fibrous Nanosilica: A Small-Angle X-Ray Scattering Perspective. *Langmuir* **2021**, *37*, 6423–6434. [CrossRef]
110. Ago, H.; Tanaka, K.; Yamabe, T.; Miyoshi, T.; Takegoshi, K.; Terao, T.; Yata, S.; Hato, Y.; Nagura, S.; Ando, N. Structural Analysis of Polyacenic Semiconductor (PAS) Materials with ^{129}xenon NMR Measurements. *Carbon* **1997**, *35*, 1781–1787. [CrossRef]
111. Simonov, P.A.; Filimonova, S.V.; Kryukova, G.N.; Moroz, E.M.; Likholobov, V.A.; Kuretzky, T.; Boehm, H.P. ^{129}Xe NMR Study of Carbonaceous Materials: Effects of Surface Chemistry and Nanotexture. *Carbon* **1999**, *37*, 591–600. [CrossRef]
112. Syamala, M.S.; Cross, R.J.; Saunders, M. ^{129}Xe NMR Spectrum of Xenon inside C60. *J. Am. Chem. Soc.* **2002**, *124*, 6216–6219. [CrossRef]
113. Romanenko, K.V.; D'Espinose De La Caillerie, J.B.; Fraissard, J.; Reshetenko, T.V.; Lapina, O.B. ^{129}Xe NMR Investigation of Catalytic Filamentous Carbon. *Microporous Mesoporous Mater.* **2005**, *81*, 41–48. [CrossRef]
114. Onfroy, T.; Guenneau, F.; Springuel-Huet, M.A.; Gédéon, A. First Evidence of Interconnected Micro and Mesopores in CMK-3 Materials. *Carbon* **2009**, *47*, 2352–2357. [CrossRef]
115. Wu, Z.; Chen, Z.; Du, X.; Logan, J.M.; Sippel, J.; Nikolou, M.; Kamaras, K.; Reynolds, J.R.; Tanner, D.B.; Hebard, A.F.; et al. Transparent Conductive Carbon Nanotube Films. *Science* **2004**, *305*, 1273–1276. [CrossRef]
116. Sadri, R.; Ahmadi, G.; Togun, H.; Dahari, M.; Kazi, S.N.; Sadeghinezhad, E.; Zubir, N. An Experimental Study on Thermal Conductivity and Viscosity of Nanofluids Containing Carbon Nanotubes. *Nanoscale Res. Lett.* **2014**, *9*, 4–13. [CrossRef]
117. Yu, M.F.; Lourie, O.; Dyer, M.J.; Moloni, K.; Kelly, T.F.; Ruoff, R.S. Strength and Breaking Mechanism of Multiwalled Carbon Nanotubes under Tensile Load. *Science* **2000**, *287*, 637–640. [CrossRef]
118. Kauffman, D.R.; Star, A. Carbon Nanotube Gas and Vapor Sensors. *Angew. Chem.-Int. Ed.* **2008**, *47*, 6550–6570. [CrossRef]
119. Clewett, C.F.M.; Pietraß, T. ^{129}Xe and 131Xe NMR of Gas Adsorption on Single- and Multi-Walled Carbon Nanotubes. *J. Phys. Chem. B* **2005**, *109*, 17907–17912. [CrossRef]
120. Romanenko, K.V.; Fonseca, A.; Dumonteil, S.; Nagy, J.B.; D'Espinose De Lacaillerie, J.B.; Lapina, O.B.; Fraissard, J. ^{129}Xe NMR Study of Xe Adsorption on Multiwall Carbon Nanotubes. *Solid State Nucl. Magn. Reson.* **2005**, *28*, 135–141. [CrossRef]
121. Oschatz, M.; Hoffmann, H.C.; Pallmann, J.; Schaber, J.; Borchardt, L.; Nickel, W.; Senkovska, I.; Rico-Francés, S.; Silvestre-Albero, J.; Kaskel, S.; et al. Structural Characterization of Micro- and Mesoporous Carbon Materials Using in Situ High Pressure ^{129}Xe NMR Spectroscopy. *Chem. Mater.* **2014**, *26*, 3280–3288. [CrossRef]

122. Wang, J.; Wang, S. Preparation, Modification and Environmental Application of Biochar: A Review. *J. Clean. Prod.* **2019**, *227*, 1002–1022. [CrossRef]
123. Akinyemi, B.A.; Adesina, A. Recent Advancements in the Use of Biochar for Cementitious Applications: A Review. *J. Build. Eng.* **2020**, *32*, 101705. [CrossRef]
124. Mauri, M.; Farina, M.; Patriarca, G.; Simonutti, R.; Klasson, K.T.; Cheng, H.N. ^{129}Xe NMR Studies of Pecan Shell-Based Biochar and Structure-Process Correlations. *Int. J. Polym. Anal. Charact.* **2015**, *20*, 119–129. [CrossRef]
125. Farina, M.; Mauri, M.; Patriarca, G.; Simonutti, R.; Klasson, K.T.; Cheng, H.N. ^{129}Xe NMR Studies of Morphology and Accessibility in Porous Biochar from Almond Shells. *RSC Adv.* **2016**, *6*, 103803–103810. [CrossRef]
126. Pekala, R.W. Organic Aerogels from the Polycondensation of Resorcinol with Formaldehyde. *J. Mater. Sci.* **1989**, *24*, 3221–3227. [CrossRef]
127. Moudrakovski, I.L.; Wang, L.Q.; Baumann, T.; Satcher, J.H.; Exarhos, G.J.; Ratcliffe, C.I.; Ripmeester, J.A. Probing the Geometry and Interconnectivity of Pores in Organic Aerogels Using Hyperpolarized ^{129}Xe NMR Spectroscopy. *J. Am. Chem. Soc.* **2004**, *126*, 5052–5053. [CrossRef]
128. Meersmann, T.; Logan, J.W.; Simonutti, R.; Caldarelli, S.; Comotti, A.; Sozzani, P.; Kaiser, L.G.; Pines, A. Exploring Single-File Diffusion in One-Dimensional Nanochannels by Laser-Polarized ^{129}Xe NMR Spectroscopy. *J. Phys. Chem. A* **2000**, *104*, 11665–11670. [CrossRef]
129. Cheng, C.Y.; Bowers, C.R. Observation of Single-File Diffusion in Dipeptide Nanotubes by Continuous-Flow Hyperpolarized Xenon-129 NMR Spectroscopy. *ChemPhysChem* **2007**, *8*, 2077–2081. [CrossRef]
130. Cheng, C.Y.; Bowers, C.R. Direct Observation of Atoms Entering and Exiting L-Alanyl-L-Valine Nanotubes by Hyperpolarized Xenon-129 NMR. *J. Am. Chem. Soc.* **2007**, *129*, 13997–14002. [CrossRef]
131. Bowers, C.R.; Dvoyashkin, M.; Salpage, S.R.; Akel, C.; Bhase, H.; Geer, M.F.; Shimizu, L.S. Squeezing Xenon into Phenylether Bis-Urea Nanochannels. *Can. J. Chem.* **2015**, *93*, 1031–1034. [CrossRef]
132. Komulainen, S.; Roukala, J.; Zhivonitko, V.V.; Javed, M.A.; Chen, L.; Holden, D.; Hasell, T.; Cooper, A.; Lantto, P.; Telkki, V.V. Inside Information on Xenon Adsorption in Porous Organic Cages by NMR. *Chem. Sci.* **2017**, *8*, 5721–5727. [CrossRef]
133. Geng, K.; He, T.; Liu, R.; Dalapati, S.; Tan, K.T.; Li, Z.; Tao, S.; Gong, Y.; Jiang, Q.; Jiang, D. Covalent Organic Frameworks: Design, Synthesis, and Functions. *Chem. Rev.* **2020**, *120*, 8814–8933. [CrossRef]
134. Ma, Y.X.; Li, Z.J.; Wei, L.; Ding, S.Y.; Zhang, Y.B.; Wang, W. A Dynamic Three-Dimensional Covalent Organic Framework. *J. Am. Chem. Soc.* **2017**, *139*, 4995–4998. [CrossRef]
135. Ma, Y.; Yu, L.; Li, H.; Zhang, S.; Wang, Z.; Wang, Y.; Chen, J. Insights into the Microstructure and Interconnectivity of Porosity in Porous Starch by Hyperpolarized ^{129}Xe NMR. *Int. J. Biol. Macromol.* **2020**, *163*, 1618–1623. [CrossRef] [PubMed]
136. Ma, Y.; Li, H.; Zhang, S.; Wang, Z.; Wang, Y.; Chen, J.; Yu, L. ^{129}Xe NMR: A Powerful Tool for Studying the Adsorption Mechanism between Mesoporous Corn Starch and Palladium. *Int. J. Biol. Macromol.* **2020**, *161*, 674–680. [CrossRef] [PubMed]
137. Wang, L.Q.; Wang, D.; Liu, J.; Exarhos, G.J.; Pawsey, S.; Moudrakovski, I. Probing Porosity and Pore Interconnectivity in Crystalline Mesoporous TiO2 Using Hyperpolarized ^{129}Xe NMR. *J. Phys. Chem. C* **2009**, *113*, 6577–6583. [CrossRef]
138. Mauri, M.; Simonutti, R. Hyperpolarized Xenon Nuclear Magnetic Resonance (NMR) of Building Stone Materials. *Materials* **2012**, *5*, 1722–1739. [CrossRef]
139. Zhou, B.; Komulainen, S.; Vaara, J.; Telkki, V.V. Characterization of Pore Structures of Hydrated Cements and Natural Shales by ^{129}Xe NMR Spectroscopy. *Microporous Mesoporous Mater.* **2017**, *253*, 49–54. [CrossRef]
140. Javed, M.A.; Komulainen, S.; Daigle, H.; Zhang, B.; Vaara, J.; Zhou, B.; Telkki, V.V. Determination of Pore Structures and Dynamics of Fluids in Hydrated Cements and Natural Shales by Various ^{1}H and ^{129}Xe NMR Methods. *Microporous Mesoporous Mater.* **2019**, *281*, 66–74. [CrossRef]
141. Filimonova, S.; Nossov, A.; Dümig, A.; Gédéon, A.; Kögel-Knabner, I.; Knicker, H. Evaluating Pore Structures of Soil Components with a Combination of "Conventional" and Hyperpolarised ^{129}Xe NMR Studies. *Geoderma* **2011**, *162*, 96–106. [CrossRef]
142. Kasavajjula, U.; Wang, C.; Appleby, A.J. Nano- and Bulk-Silicon-Based Insertion Anodes for Lithium-Ion Secondary Cells. *J. Power Sources* **2007**, *163*, 1003–1039. [CrossRef]
143. Mao, Y.; Kim, D.; Joo, J.; Sailor, M.J.; Hopson, R.; Wang, L.Q. Hyperpolarized ^{129}Xe Nuclear Magnetic Resonance Study of Mesoporous Silicon Sponge Materials. *J. Mater. Res.* **2017**, *32*, 3038–3045. [CrossRef]
144. Mao, Y.; Kim, D.; Hopson, R.; Sailor, M.J.; Wang, L.Q. Investigation of Grafted Mesoporous Silicon Sponge Using Hyperpolarized ^{129}Xe NMR Spectroscopy. *J. Mater. Res.* **2018**, *33*, 2637–2645. [CrossRef]
145. Brock, S.L.; Arachchige, I.U.; Kalebaila, K.K. Metal Chalcogenide Gels, Xerogels and Aerogels. *Comments Inorg. Chem.* **2006**, *27*, 103–126. [CrossRef]
146. Pawsey, S.; Kalebaila, K.K.; Moudrakovski, I.; Ripmeester, J.A.; Brock, S.L. Pore Structure and Interconnectivity of CdS Aerogels and Xerogels by Hyperpolarized Xenon NMR. *J. Phys. Chem. C* **2010**, *114*, 13187–13195. [CrossRef]
147. Besghini, D.; Mauri, M.; Simonutti, R. Time Domain NMR in Polymer Science: From the Laboratory to the Industry. *Appl. Sci.* **2019**, *9*, 1801. [CrossRef]
148. Brouwer, D.H.; Alavi, S.; Ripmeester, J.A. A Double Quantum ^{129}Xe NMR Experiment for Probing Xenon in Multiply-Occupied Cavities of Solid-State Inclusion Compounds. *Phys. Chem. Chem. Phys.* **2007**, *9*, 1093–1098. [CrossRef] [PubMed]
149. Tallavaara, P.; Telkki, V.V.; Jokisaari, J. Behavior of a Thermotropic Nematic Liquid Crystal Confined to Controlled Pore Glasses as Studied by ^{129}Xe NMR Spectroscopy. *J. Phys. Chem. B* **2006**, *110*, 21603–21612. [CrossRef]

150. Tallavaara, P.; Jokisaari, J. 2D ^{129}Xe EXSY of Xenon Atoms in a Thermotropic Liquid Crystal Confined to a Controlled-Pore Glass. *Phys. Chem. Chem. Phys.* **2006**, *8*, 4902–4907. [CrossRef]
151. Truxal, A.E.; Slack, C.C.; Gomes, M.D.; Vassiliou, C.C.; Wemmer, D.E.; Pines, A. Nondisruptive Dissolution of Hyperpolarized ^{129}Xe into Viscous Aqueous and Organic Liquid Crystalline Environments. *Angew. Chem.-Int. Ed.* **2016**, *55*, 4666–4670. [CrossRef]
152. Keenan, C.D.; Herling, M.M.; Siegel, R.; Petzold, N.; Bowers, C.R.; Rössler, E.A.; Breu, J.; Senker, J. Porosity of Pillared Clays Studied by Hyperpolarized ^{129}Xe NMR Spectroscopy and Xe Adsorption Isotherms. *Langmuir* **2013**, *29*, 643–652. [CrossRef]
153. Utiu, L.; Filipoi, C.; Demco, D.E.; Zhu, X.; Vinokur, R.; Conradi, O.; Graichen, A.; Blümich, B.; Möller, M. Free Volume of Poly(Perfluorosulfonic Acid)/SiO2 Composite Proton Exchange Membranes by ^{129}Xe NMR. *Chem. Phys. Lett.* **2011**, *506*, 71–75. [CrossRef]
154. Zaheer, M.; Keenan, C.D.; Hermannsdörfer, J.; Roessler, E.; Motz, G.; Senker, J.; Kempe, R. Robust Microporous Monoliths with Integrated Catalytically Active Metal Sites Investigated by Hyperpolarized ^{129}Xe NMR. *Chem. Mater.* **2012**, *24*, 3952–3963. [CrossRef]
155. Wang, L.Q.; Wang, D.; Liu, J.; Exarhos, G.J. Probing Porosity and Pore Interconnectivity in Self-Assembled TiO_2-Graphene Hybrid Nanostructures Using Hyperpolarized ^{129}Xe NMR. *J. Phys. Chem. C* **2012**, *116*, 22–29. [CrossRef]
156. Burueva, D.B.; Pokochueva, E.V.; Wang, X.; Filkins, M.; Svyatova, A.; Rigby, S.P.; Wang, C.; Pavlovskaya, G.E.; Kovtunov, K.V.; Meersmann, T.; et al. In Situ Monitoring of Heterogeneous Catalytic Hydrogenation via ^{129}Xe NMR Spectroscopy and Proton MRI. *ACS Catal.* **2020**, *10*, 1417–1422. [CrossRef]